Prediction of the pressure distribution on a cubical building with implicit LES

D.A. Köse and E. Dick

Department of Flow, Heat and Combustion Mechanics, Ghent University
Sint–Pietersnieuwstraat 41, 9000 Gent – Belgium
E–mail: DemirAli.Kose@Ugent.be, Erik.Dick@Ugent.be

Abstract: **This paper presents a numerical study of the flow around a cubical building in an atmospheric boundary layer. The Reynolds number of the flow is Re = 4.10^6. Different types of turbulence models, steady state RANS, hybrid RANS/LES and LES, are used and the simulation results are compared to field measurement data of the mean pressure distribution. The objective is to build an approach to perform simulations on coarse grids with low computational cost. The outcome is that the Implicit LES (ILES) method is the most accurate for coarse grid simulations. In order to verify the sensitivity of the results to the Reynolds number, also simulations of a wind tunnel experiment at Reynolds number 4.10^4 are performed. We demonstrate that also for lower Reynolds numbers, although not optimal, the ILES approach leads to quite good results.**

Keywords: **ILES, buildings, pressure distribution**

1 INTRODUCTION

Despite the continuing increase in computational power, fully resolved Large Eddy Simulation (LES) of high Reynolds number flows, such as flows around buildings, is nowadays not feasible. In LES, large structures in the flow are resolved while the effects of structures smaller than a cut–off length related to the computational cell size are modelled. The influence of the modelled scales on the resolved part of the flow is accounted for by a sub–grid scale model (SGS). The higher the Reynolds number, the higher the amount of grid points needed to adequately resolve the flow. A sufficiently resolved simulation of the flow around a real size building would require several tens of millions of grid points. For instance, Lim et al. (2009) simulated the flow around a surface mounted cube placed in a turbulent boundary layer and compared to measurements. Their results confirm the conclusion that LES is a viable tool for use in wind engineering problems. They used a uniform grid containing approximately ten million cells with grid spacing h/32 (h is the cube height). The Reynolds number was 20,000. In order to go to realistic Reynolds numbers, in the order of a few millions, one needs much finer grids. This is not feasible at all. Therefore, in practice, RANS models are typically used in the analysis of flows around buildings. RANS models allow much coarser grids because they average flow features over the largest length scale of the turbulence. The drawback is that the flow is represented much steadier than in reality. In particular, flows around buildings are extremely unsteady. Quasi–steady turbulence models are therefore not capable of capturing the main unsteadiness of these flows. Mean velocity profiles, drag and other quantities predicted with RANS models deviate considerably from experimental data (Rodi, 1997). RANS models have been be modified in order to improve their predictive qualities for wind engineering applications (Lun et al., 2007), but even with highly improved RANS models, the predictions of the flow field around a building remain poor (Murakami et al., 1997; Tominaga et al., 2008). Another option is to use hybrid turbulence models. In such models, the best qualities of RANS (coarse grid, low computational cost) and LES (accuracy) are combined: near walls (e.g. the building surface) the hybrid model is in RANS–mode while further away the LES SGS model is active. Predictions with hybrid models are in much better agreement with experimental data than RANS results (Roy et al., 2003; Hanjalic and Kenjeres, 2008). However, for reliable predictions, hybrid models require much finer grids than RANS models. For practical use in building flows, the associated computational cost is still too high.

In this paper, we aim at developing a low cost simulation technique, which means using a coarse grid, as typical in a RANS simulation, so of the order of 1 million grid cells. In section 2, we describe the different turbulence models that we test: RANS, LES and hybrid RANS/LES. In section 3, we present the results of the flow around a cube in a channel, at relatively low Reynolds number. The aim of this study is to determine which model gives the best velocity and pressure predictions on coarse grids. The observation is that for low Reynolds number, a hybrid RANS/LES model is optimal. However, we also observe that the results of coarse grid LES are also quite acceptable, provided that an adequate wall model is used. In section 4, the best models are then applied to the flow around a cubical building in an atmospheric boundary layer. The Reynolds number is 4 million, based on the building height and the velocity of the approaching flow at building height level. Pressure coefficients on a horizontal and a vertical section are available from measurements (Richards et al., 2001) and are compared with the simulation results. For such a high Reynolds number, the results of hybrid RANS/LES and RANS do not differ much on a very coarse grid and are of bad quality. So, the hybrid technique, which we found to be optimal for the low Reynolds number flows, cannot be extended to high Reynolds number flows, when the grid is very coarse. We show that LES without any sub–grid model, so Implicit LES, but combined with an adequate wall model, leads to quite good results.

2 TURBULENCE MODELS

Different models are tested. All simulations have been performed with the commercial CFD package FLUENT, version 6.3 (2006). Most of the models are standard available in the package.

2.1. RANS models

2.1.1. The standard k–ε model

The transport equations for the turbulent kinetic energy k and its dissipation rate ε are

$$\frac{\partial}{\partial t}\left(\rho k\right)+\frac{\partial}{\partial x_i}\left(\rho k u_i\right)=\frac{\partial}{\partial x_i}\left[\left(\mu+\frac{\mu_t}{\sigma_k}\right)\frac{\partial k}{\partial x_i}\right]+G_k-Y_k\,, \tag{1}$$

$$\frac{\partial}{\partial t}\left(\rho \varepsilon\right)+\frac{\partial}{\partial x_i}\left(\rho \varepsilon u_i\right)=\frac{\partial}{\partial x_i}\left[\left(\mu+\frac{\mu_t}{\sigma_\varepsilon}\right)\frac{\partial \varepsilon}{\partial x_i}\right]+G_\varepsilon-Y_\varepsilon\,. \tag{2}$$

The density of the fluid ρ is taken as a constant. The production of turbulent kinetic energy G_k is computed consistent with the Boussinesq hypothesis by

$$G_k = \mu_t S^2\,, \tag{3}$$

where S is the modulus of the mean rate–of–strain tensor, defined as

$$S \equiv \sqrt{2 S_{ij} S_{ij}} \ \ \text{with} \ \ S_{ij} = \frac{1}{2}\left(\frac{\partial u_i}{\partial x_j}+\frac{\partial u_j}{\partial x_i}\right). \tag{4}$$

The turbulent viscosity μ_t is computed from k and ε as

$$\mu_t = \rho C_\mu \frac{k^2}{\varepsilon}. \tag{5}$$

The dissipation term in the k–equation is $Y_k = \rho\varepsilon$. The production and dissipation terms in the ε–equation are

$$G_\varepsilon = C_{1\varepsilon} \frac{\varepsilon}{k} G_k \text{ and } Y_\varepsilon = C_{2\varepsilon} \rho \frac{\varepsilon^2}{k}. \tag{6}$$

The model constants are $C_\mu = 0.09$, $C_{1\varepsilon} = 1.44$, $C_{2\varepsilon} = 1.92$, $\sigma_k = 1.0$, $\sigma_\varepsilon = 1.3$.

2.1.2. The realizable k–ε model

The transport equation for k is the same as in the standard k–ε model, with the production term also calculated in the same way.

The transport equation for ε has the same form as in the standard model, but production and dissipation terms are now given by

$$G_\varepsilon = \rho C_1 S \varepsilon \text{ and } Y_\varepsilon = \rho C_2 \frac{\varepsilon^2}{k + \sqrt{v\varepsilon}}, \tag{7}$$

with $C_1 = \max\left[0.43, \frac{\eta}{\eta+5}\right]$ and $\eta = S\frac{k}{\varepsilon}$.

The turbulent viscosity μ_t is computed from

$$C_\mu = \frac{1}{A_0 + A_S \dfrac{kU^*}{\varepsilon}}, \tag{8}$$

with $A_0 = 4.04$ and $U^* = \sqrt{S_{ij}S_{ij} + \Omega_{ij}\Omega_{ij}}$, where $\Omega_{ij} = \frac{1}{2}\left(\frac{\partial u_i}{\partial x_j} - \frac{\partial u_j}{\partial x_i}\right)$, and $A_S = \sqrt{6}\cos\phi$, with

$\phi = \frac{1}{3}\cos^{-1}\left(\sqrt{6}W\right)$, where $W = \frac{S_{ij}S_{ik}S_{ki}}{S^3}$.

The model constants are $\sigma_k = 1.0$, $\sigma_\varepsilon = 1.2$, $C_2 = 1.9$.

2.1.3. The k–ω SST model

The transport equation for k has the same form as in the standard k–ε model. The transport equation for the specific dissipation rate ω is

$$\frac{\partial}{\partial t}(\rho\omega) + \frac{\partial}{\partial x_i}(\rho\omega u_i) = \frac{\partial}{\partial x_i}\left[\left(\mu + \frac{\mu_t}{\sigma_\omega}\right)\frac{\partial\omega}{\partial x_i}\right] + G_\omega - Y_\omega + D_\omega. \tag{9}$$

The production and dissipation terms of turbulent kinetic energy are

$$G_k = \min\left(\mu_t S^2, 10\rho\beta^* k\omega\right) \text{ and } Y_k = \rho\beta^* k\omega. \tag{10}$$

The specific dissipation ω is related to the dissipation ε by $\omega = \dfrac{\varepsilon}{\beta^* k}$.

The production and dissipation terms of ω are

$$G_\omega = \frac{\alpha}{\nu_t}\tilde{G}_k \text{ and } Y_\omega = \rho\beta\omega^2 . \tag{11}$$

The cross term in the dissipation equation is

$$D_\omega = 2\left(1 - F_1\right)\rho\sigma_{\omega,2}\frac{1}{\omega}\frac{\partial k}{\partial x_i}\frac{\partial \omega}{\partial x_i}, \tag{12}$$

where $\sigma_{\omega,2}$ is a constant and $F_1 = \tanh\left(\Phi_1^4\right)$ is a blending function with

$$\Phi_1 = \min\left[\max\left(\frac{\sqrt{k}}{0.09\omega y}, \frac{500\mu}{\rho y^2 \omega}\right), \frac{4\rho k}{\sigma_{\omega,2}D_\omega^+ y^2}\right], \tag{13}$$

where $D_\omega^+ = \max\left[2\rho\dfrac{1}{\sigma_{\omega,2}}\dfrac{1}{\omega}\dfrac{\partial k}{\partial x_j}\dfrac{\partial \omega}{\partial x_j}, 10^{-10}\right]$ and $\sigma_{\omega,2} = 1.168$.

Finally, the turbulent viscosity μ_t is computed as

$$\mu_t = \frac{\rho k}{\omega}\frac{1}{\max\left[\dfrac{1}{\alpha^*}, \dfrac{SF_2}{a_1\omega}\right]} . \tag{14}$$

In this expression, $a_1 = 0.31$ and $F_2 = \tanh\left(\Phi_2^2\right)$ is a blending function, with

$$\Phi_2 = \max\left[2\frac{\sqrt{k}}{0.09\omega y}, \frac{500\mu}{\rho y^2 \omega}\right]. \tag{15}$$

The model factors $\beta, \sigma_k, \sigma_\varepsilon$ are interpolated as

$$\beta = F_1\beta_1 + \left(1 - F_1\right)\beta_2 \text{ and } \sigma = \frac{1}{F_1/\sigma_1 + \left(1 - F_1\right)/\sigma_2} \tag{16}$$

with $\beta_1 = 0.075$, $\beta_2 = 0.0828$, $\sigma_{k,1} = 1.176$, $\sigma_{k,2} = 1.0$, $\sigma_{\omega,1} = 2.0$, $\sigma_{\omega,2} = 1.0$.

The model constants are $\beta^* = 0.09$, $\alpha = \alpha^* = 1$.

2.2. LES and implicit LES models

The filtered Navier–Stokes equations for a constant density fluid are

$$\frac{\partial \overline{u}_i}{\partial x_i} = 0,$$ (17)

$$\frac{\partial}{\partial t}\left(\rho \overline{u}_i\right) + \frac{\partial}{\partial x_j}\left(\rho \overline{u}_i \overline{u}_j\right) = \frac{\partial \overline{\sigma}_{ij}}{\partial x_j} - \frac{\partial \overline{p}}{\partial x_i} - \frac{\partial \tau_{ij}}{\partial x_j}.$$ (18)

Filtered quantities are denoted by an overbar. σ_{ij} is the filtered molecular viscosity stress tensor and τ_{ij} is the sub–grid scale stress tensor resulting from the filtering operation: $\tau_{ij} = \rho \overline{u_i u_j} - \rho \overline{u}_i \overline{u}_j$.

Strictly, the equations (17) and (18) are only correct for constant filter width. This means that for spatially varying filter width, the spatial commutation errors that generate supplementary terms in the equations are neglected (Ghosal and Moin, 1995), as is commonly done in practically oriented work.

The sub–grid scale stress tensor is modelled by

$$\tau_{ij} - \frac{1}{3}\tau_{kk}\delta_{ij} = -2\mu_t \overline{S}_{ij},$$ (19)

where μ_t is the sub–grid eddy viscosity and $\overline{S}_{ij}$ the rate–of–strain tensor calculated with the filtered velocity components. The sub–grid eddy viscosity has to be further modelled. The isotropic part of the stresses is not modelled but added to the pressure term.

2.2.1. The standard Smagorinsky–Lilly model

In the Smagorinsky–Lilly model, the eddy viscosity is obtained from

$$\mu_t = \rho L_S^2 \left|\overline{S}\right|,$$ (20)

where $\left|\overline{S}\right| \equiv \sqrt{2\overline{S}_{ij}\overline{S}_{ij}}$ and L_S is the mixing length for sub–grid scales, computed by

$$L_S = \min\left(\kappa d, C_S \overline{\Delta}\right),$$ (21)

where κ is the von Karman constant, d is the distance to the closest wall, C_S is the Smagorinsky constant equal to 0.1 and $\overline{\Delta}$ is the filter width. The filter width is calculated by $\overline{\Delta} = V^{1/3}$, where V is the volume of the computational cell.

2.2.2. The dynamic Smagorinsky–Lilly model

The model factor C_S in the Smagorinsky–Lilly model is not a universal constant and has an optimal value which varies from flow to flow. The dynamic procedure by Germano et al. (1991) and Lilly (1992)

allows adapting the factor to the local flow circumstances. The model factor is dynamically computed based on the information provided by the resolved scales of motion.

A test–filter, denoted by a caret, is applied to the filtered equations in order to remove the smallest scales of the resolved field. Application of a test–filter to the Navier–Stokes equations (17–18) leads to

$$\frac{\partial \hat{\bar{u}}_i}{\partial x_i} = 0, \tag{22}$$

$$\frac{\partial}{\partial t}(\rho \hat{\bar{u}}_i) + \frac{\partial}{\partial x_j}(\rho \hat{\bar{u}}_i \hat{\bar{u}}_j) = \frac{\partial \hat{\bar{\sigma}}_{ij}}{\partial x_j} - \frac{\partial \hat{\bar{p}}}{\partial x_i} - \frac{\partial T_{ij}}{\partial x_j}, \tag{23}$$

where T_{ij} is the sub–test scale stress tensor:

$$T_{ij} = \rho \widehat{\overline{u_i u_j}} - \rho \hat{\bar{u}}_i \hat{\bar{u}}_j. \tag{24}$$

The fundamental concept of the dynamic modelling is the assumption that T_{ij} is similar to τ_{ij}, so that T_{ij} can be modelled in the same way as τ_{ij} by

$$T_{ij} - \frac{1}{3}\delta_{ij}T_{kk} = -2\rho C \hat{\Delta}^2 \left|\hat{\bar{S}}\right| \hat{\bar{S}}_{ij}, \text{ with } C = C_s^2, \tag{25}$$

where $\hat{\Delta}$ is the test–filter width. The same coefficient C_S is used in the models of both stress tensors.

Test–filtering the sub–grid scale stress tensor and subtracting it from T_{ij} results in

$$L_{ij} = T_{ij} - \hat{\tau}_{ij} = \rho \widehat{\overline{u_i u_j}} - \rho \hat{\bar{u}}_i \hat{\bar{u}}_j - \left(\rho \widehat{\overline{u_i u_j}} - \rho \widehat{\overline{u}_i \overline{u}_j} \right) = \rho(\widehat{\overline{u_i u_j}} - \hat{\bar{u}}_i \hat{\bar{u}}_j). \tag{26}$$

The Leonard stresses L_{ij} can be interpreted as associated with the resolved scales between the test–filter scale $\hat{\Delta}$ and the grid filter scale $\bar{\Delta}$.

In terms of the models for T_{ij} and τ_{ij}, one obtains

$$L_{ij} - \frac{1}{3}\delta_{ij}L_{kk} = -2\rho C \hat{\Delta}^2 \left|\hat{\bar{S}}\right| \hat{\bar{S}}_{ij} + 2\rho \widehat{C \bar{\Delta}^2 \left|\bar{S}\right| \bar{S}_{ij}}. \tag{27}$$

Using the assumption that $C\bar{\Delta}^2$ is only weakly varying in space, it is taken out of the test–filter operation, leading to

$$L_{ij} - \frac{1}{3}\delta_{ij}L_{kk} = -2\rho C \hat{\Delta}^2 \left|\hat{\bar{S}}\right| \hat{\bar{S}}_{ij} + 2\rho C \bar{\Delta}^2 \widehat{\left|\bar{S}\right| \bar{S}_{ij}} = C M_{ij}, \tag{28}$$

where the right hand side in (28) is written as the model factor C, which has to be determined, and a factor M_{ij} which is calculated from filtered velocity data. The model factor C is obtained by minimizing the difference between the left and right hand sides in (28) in a least squares sense, leading to

$$C = C_s^2 = \frac{L_{ij}M_{ij}}{M_{ij}M_{ij}} . \tag{29}$$

The numerator in (29) can become negative. This is inconsistent with the relationship $C = C_s^2$. Further, allowing a negative value of C in the sub–grid eddy viscosity, which is technically possible, causes numerical instability. To avoid this, C is clipped at 0. C_S is also clipped at the positive side to 0.23.

The width of the test–filter should be larger than the width of the grid filter. The test–filter should also be applicable to unstructured meshes. In the Fluent package, the grid filter operator is averaging over the cell, as a consequence of the finite volume discretization. A consistent test–filter is averaging over the cell and the neighbouring cells, as shown in figure 1.
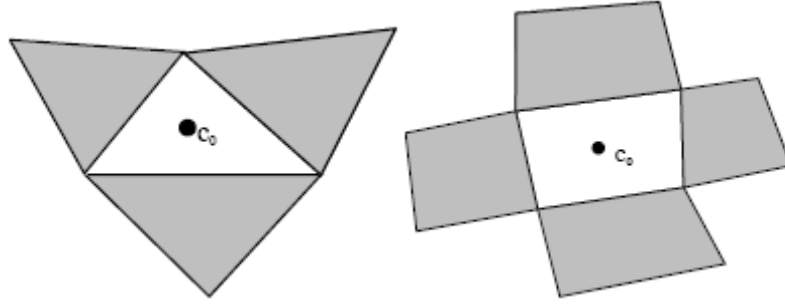

Figure 1: Computational cells involved in the test–filter operation, left: triangular mesh; right: quadrilateral mesh.

2.2.3. The dynamic kinetic energy SGS model

The dynamic sub–grid scale kinetic energy model in the Fluent package is the model proposed by Kim and Menon (1997). In this model, a transport equation is solved for the sub–grid scale kinetic energy:

$$\frac{\partial}{\partial t}(\rho k_{sgs}) + \frac{\partial_i}{\partial x_i}(\rho k_{sgs}\overline{u}_i) = \frac{\partial}{\partial x_i}\left[\left(\mu + \frac{\mu_t}{\sigma_k}\right)\frac{\partial k_{sgs}}{\partial x_i}\right] - \tau_{ij}\frac{\partial \overline{u}_i}{\partial x_j} - \rho \varepsilon_{sgs} , \tag{30}$$

where σ_k is equal to 1 and

$$k_{sgs} = \frac{1}{2}\left(\overline{u_k^2} - \overline{u}_k^2\right) \text{ and } \tau_{ij} = \rho(\overline{u_i u_j} - \overline{u}_i\overline{u}_j) . \tag{31}$$

The sub–grid tensor τ_{ij} is modelled as

$$\tau_{ij} - \frac{2}{3}\delta_{ij}k_{sgs} = -2\mu_t \overline{S}_{ij} = -2\rho C_\tau \overline{\Delta} k_{sgs}^{1/2}\overline{S}_{ij} , \tag{32}$$

with $\overline{\Delta}$ the grid filter width.

The dissipation term is modelled as

$$\varepsilon_{sgs} = C_\varepsilon k_{sgs}^{3/2} / \overline{\Delta} . \tag{33}$$

The model constants C_ε and C_τ are determined dynamically in the same style as discussed for the dynamic Smagorinsky–Lilly model. The Leonard stresses are defined according to (26) and by the trace of the tensor L_{ij}, an expression for the kinetic energy resolved at the test level, k_{test}, is obtained:

$$\rho k_{test} = \frac{1}{2}\rho(\widehat{\overline{u_k}\overline{u_k}} - \hat{\bar{u}}_k\hat{\bar{u}}_k) = \frac{L_{kk}}{2}.$$
(34)

The production of k_{test} is given by $-L_{ij}\left(\dfrac{\partial \hat{\bar{u}}_i}{\partial x_j}\right)$ and its dissipation by

$$\rho e = (\mu + \mu_t)\left(\frac{\widehat{\partial \overline{u}_i}}{\partial x_j}\frac{\partial \overline{u}_i}{\partial x_j} - \frac{\partial \hat{\bar{u}}_i}{\partial x_j}\frac{\partial \hat{\bar{u}}_i}{\partial x_j}\right).$$
(35)

The Leonard stress tensor is modelled as

$$L_{ij} - \frac{1}{3}\delta_{ij}L_{kk} = -2\rho C_\tau \hat{\bar{\Delta}} k_{test}^{1/2} \hat{\bar{S}}_{ij} = C_\tau \Sigma_{ij},$$
(36)

where Σ_{ij} is computed from data on the test level.

The coefficient C_τ is determined by least square minimizing the difference between left and right hand sides in (36), resulting in

$$C_\tau = \frac{L_{ij}\Sigma_{ij}}{\Sigma_{ij}\Sigma_{ij}}.$$
(37)

A similarity assumption between ε_{sgs} and e is adopted to obtain an expression for C_ε:

$$e = C_\varepsilon k_{test}^{3/2} / \hat{\bar{\Delta}}.$$
(38)

The value of C_ε is obtained by inserting the values of k_{test} and e from (34) and (35).

2.2.4. Implicit LES

In this case, no SGS model is used. This is achieved by bringing the Smagorinsky constant C_S equal to 0 in the standard model. The influence of the unresolved scales on the resolved ones is accounted for by the numerical dissipation of the discretization scheme of the convective terms in the momentum equations. The implicit LES method has gained popularity in recent years (Grinstein and Drikakis, 2007), particularly for external flows around buildings (Patnik et al, 2007). The essential feature is that the numerical dissipation mimics sufficiently well the physical process of dissipation of the turbulent eddies.

For this purpose, we here apply a TVD–discretization, in particular the bounded central scheme. In this scheme, a transported variable on a face of a cell is defined as the value in the node on the upwind side plus an increment. The basic value of the increment is half the difference between the value in the upwind node and the value in the downwind node. So, if the increment is added without modification, the central discretization scheme is obtained. The basic increment is compared to half of the difference between node

values shifted in the upwind sense. If the sign of the basic increment and the sign of the upwind increment differ, the increment that is added to the upwind node value to obtain the face value is set to zero. Then, the scheme becomes a first order upwind scheme. This means that small scale oscillations in the transported quantity are strongly damped. If the sign of the basic increment and the sign of the upwind increment are the same, then the absolute value of the increment that is added to the upwind node value to obtain the face value is limited to twice the absolute value of the upwind increment. This means that large scale oscillations are weakly damped, where the damping becomes stronger if the wavelength of the oscillation becomes smaller. So, we understand that the bounding mechanism or TVD mechanism of the scheme acts as a sub–grid scale dissipation mechanism in the sense as wanted in a LES. It is clearly a non–linear mechanism that is quite difficult to express in the conventional way of a dissipation term of higher order. The bounded central scheme is one of the simplest schemes satisfying the requirements for non–oscillatory behaviour in the Sweby–diagram (Sweby, 1984) or in the normalised variable diagram (NVD) of Leonard (Leonard, 1991).

2.3. Hybrid RANS/LES models

In a hybrid approach, the unsteady RANS equations are employed in near–wall regions, while the filtered versions of the Navier–Stokes equations are used in the regions away from walls. In the Fluent package, the hybrid models are of so–called DES (detached eddy simulation) type. This means that a RANS model is adapted to serve as sub–grid model in the zones away from walls, treated in LES–mode, where the eddy structures are detached.

2.3.1. The DES k–ε model

The transport equations for k and ε of the realizable k–ε model are used to model the eddy viscosity in the RANS zones and to model the sub–grid viscosity in the LES zones.

In the hybrid formulation, the dissipation term in the equation for k is computed from

$$Y_k = \rho k^{3/2} / \ell_{des}, \tag{39}$$

where $\ell_{des} = \min\left(\ell_{rke}, \ell_{les}\right)$, $\ell_{rke} = k^{3/2} / \varepsilon$, $\ell_{les} = C_{des}\Delta$ and $\Delta = \max\left(\Delta x, \Delta y, \Delta z\right)$, the maximum grid spacing. The standard value of C_{des} is 0.65.

2.3.2. The DES k–ω SST model

This model is based on the k–ω SST model. The dissipation term of the turbulent kinetic energy is modified into (39), where $\ell_{des} = \min\left(\ell_{k\omega}, \ell_{les}\right)$, $\ell_{k\omega} = k^{1/2} / (\beta^*\omega)$, and $\ell_{les} = C_{des}\Delta$, as in the previous model.

2.3.3. The DES k–ℓ model

The k–ℓ one equation model is employed to obtain the turbulent eddy viscosity. For the SGS viscosity the sub–grid scale k_{sgs}–ℓ model of Yoshizawa (1993) and Fureby (1999) is used.

The equation for turbulent kinetic energy, is the standard one (1), with the production term computed as $G_k = \mu_t S^2$, and the dissipation term as $Y_k = C_\varepsilon k^{3/2} / \ell_\varepsilon$.

The turbulent viscosity μ_t is computed as

$$\mu_t = \rho\, C_\mu \ell_\mu k^{1/2}. \tag{40}$$

The length scales ℓ_μ and ℓ_ε are

$$\ell_\mu = \min\left(2.4y\left(1-e^{-0.016\,\mathrm{Re}_y}\right),\overline{\Delta}\right),\ \ell_\varepsilon = \min\left(2.4y\left(1-e^{-0.263\,\mathrm{Re}_y}\right),\overline{\Delta}\right), \tag{41}$$

with $\overline{\Delta} = V^{\frac{1}{3}}$, the cube root of the cell volume, and

$$\mathrm{Re}_y = y\frac{\rho k^{1/2}}{\mu}, \tag{42}$$

with y the distance to the closest wall.

In the LES region, C_μ = 0.07 and C_ε = 1.05, while in the RANS region C_μ = 0.09 and C_ε = 1. The DES k–ℓ model had to be programmed with user defined functions (UDF's) since the model is not available in the Fluent package.

2.4. Wall models

2.4.1. Enhanced Wall Treatment in Fluent

The wall treatment by Fluent for RANS and hybrid RANS/LES consists of two parts. Firstly, for the k–ε type models, in wall vicinity, the eddy viscosity is obtained from a one–equation k–ℓ model, independent of the chosen model which is used further away. This two–layer approach is called enhanced wall treatment. By this two–layer approach, the low Reynolds number functions, typically necessary to adapt a k–ε model in wall vicinity, are avoided. A similar treatment is not necessary for k–ω type models. Secondly, the wall shear stress is computed from a blending between a near–wall viscous value and a logarithmic law value. The obtained formula is called the enhanced wall function. This last treatment is applied to all models.

The two–layer approach

The whole domain is subdivided into a viscosity–affected region and a fully–turbulent region. The wall–distance based turbulent Reynolds number Re_y (42) determines the demarcation of the two regions. The one–equation model of Wolfstein (1969) is used in the viscosity–affected region (Re_y < 200). The k–equation in this model is the same as in the k–ω model of Yoshizawa and Fureby, discussed above. The turbulent viscosity μ_t, which we denote here by $\mu_{t,wall}$, is computed from (40). The model constants are C_μ = 0.09 and C_ε = 1. The length scales ℓ_μ and ℓ_ε are defined as

$$l_\mu = yC_l^*\left(1-e^{-\mathrm{Re}_y/70}\right),\ l_\varepsilon = yC_l^*\left(1-e^{-\mathrm{Re}_y/2C_l^*}\right), \tag{43}$$

where C_l^* is a constant equal to $C_l^* = \kappa C_\mu^{-3/4} = 2.495$

In the enhanced wall treatment, the two–layer definition is smoothly blended with the high Reynolds–number definition from the outer region by

$$\mu_{t,enh} = \lambda_\mu \mu_t + \left(1 - \lambda_\mu\right) \mu_{t,wall}. \tag{44}$$

The blending function λ_μ is defined such that it is equal to unity far from walls and approaches zero very near to walls. The blending function is given by

$$\lambda_\mu = \frac{1}{2}\left[1 - \tanh\left(\frac{\mathrm{Re}_y - \mathrm{Re}_y^*}{A}\right)\right] \text{ with } A = \frac{\left|\Delta\mathrm{Re}_y\right|}{\tanh(0.98)}. \tag{45}$$

The value of $\Delta\mathrm{Re}_y$ can be chosen between 10 and 40. It has the value of 40 in Fluent.

The enhanced wall function for RANS and DES

The law of the wall is reformulated to be applicable throughout the near–wall region. This is achieved by blending the linear and logarithmic expressions using the blending functions of Kader (1981):

$$u^+ = e^{-\Gamma} u_{lam}^+ + e^{-1/\Gamma} u_{turb}^+, \tag{46}$$

where $u^+ = u / u_\tau$ with the friction velocity $u_\tau = \sqrt{\tau_w / \rho}$.

The blending function Γ is given by

$$\Gamma = \frac{0.01\left(y^+\right)^4}{1 + 5y^+}, \tag{47}$$

where $y^+ = y u_\tau / \nu$.

The expression for the derivative $\dfrac{du^+}{dy^+}$ is

$$\frac{du^+}{dy^+} = e^{-\Gamma} \frac{du_{lam}^+}{dy^+} + e^{-1/\Gamma} \frac{du_{turb}^+}{dy^+}. \tag{48}$$

The laminar law–of–the–wall is determined from $\dfrac{du_{lam}^+}{dy^+} = 1 + \alpha y^+$ where α expresses the pressure gradient effect. Integration results in $u_{lam}^+ = y^+\left(1 + \dfrac{\alpha}{2} y^+\right)$. The enhanced turbulent law–of–the–wall is based on the approaches of White and Christoph (1971) and Huang et al. (1993). In absence of thermal effects, the expression is given by $\dfrac{du_{turb}^+}{dy^+} = \dfrac{1}{\kappa y^+}\sqrt{S'}$ where $S' = 1 + \alpha y^+$ if $y^+ < y_s^+$, and $S' = 1 + \alpha y_s^+$ if $y^+ \geq y_s^+$, with $y_s^+ = 60$. Integrating the expression above gives u_{turb}^+.

The approach guarantees the correct asymptotic behaviour for large and small values of y^+ and a reasonable representation of velocity profiles when y^+ falls inside the wall buffer region ($3 < y^+ < 10$).

The boundary condition for turbulent kinetic energy is $\partial k / \partial n = 0$ and the production of turbulent kinetic energy G_k is computed using the velocity gradient from the blended law–of–the–wall (48). The value of the friction velocity u_τ is obtained from the expression of u^+ (46), which constitutes an implicit equation in u_τ. The velocity gradient follows from

$$\frac{du}{dy} = \frac{u_\tau^2}{\nu}\frac{du^+}{dy^+} . \tag{49}$$

2.4.2. An alternative wall model for RANS and DES

The procedure to calculate the wall shear stress and the production term in the turbulent kinetic energy equation can be made explicit with the approach of Popovac and Hanjalic (2007).

The shear stress at the wall is computed using a blending of viscous τ_w^v and turbulent τ_w^t expressions. In the viscous sublayer,

$$\tau_w^v = \mu U_p / y_p , \tag{50}$$

where the subscript p expresses that we take the values of the velocity parallel to the wall and the distance to the wall in the centre of the first cell adjacent to the wall. The expression is only valid for small values of y^+.

If the centre of the first cell is located in the logarithmic layer, we derive from $u^+ = u / u_\tau$ and $y^+ = y u_\tau / \nu$:

$$\frac{y^+}{u^+} = \frac{u_\tau^2 y}{u\nu} = \frac{\tau_w y}{u\mu} , \tag{51}$$

so that

$$\tau_w^t = \mu \frac{U_p}{y_p}\frac{y^+}{u^+} . \tag{52}$$

We write the logarithmic law as

$$u^+ = \frac{1}{\kappa}\log\left(y^+\right) + B = \frac{1}{\kappa}\log\left(Ey^+\right), \text{ with E} = 9.793. \tag{53}$$

This gives

$$\tau_w^t = \mu \frac{U_p}{y_p}\left[\frac{\kappa y_p^+}{\log\left(Ey_p^+\right)}\right]. \tag{54}$$

We then take as blending

$$\tau_w = \tau_w^v e^{-\Gamma} + \tau_w^t e^{-1/\Gamma} , \tag{55}$$

with the blending function Γ computed by (47). However, in the expressions (47) and (54), y^+ or y_p^+ is replaced by the equivalent quantity $y_p^* = \dfrac{\rho C_\mu^{1/4} k_p^{1/2}}{\mu} y_p$. The wall model is insensitive to the exact position of the near–wall cell centre. In addition, this model is easy to implement.

The velocity derivative necessary for the production term in the equation for turbulent kinetic energy is calculated in the same way as for the enhanced wall function approach of Fluent, but with y^+ replaced by y_p^*. The wall model is programmed with UDF's. In what follows, we call this wall model our own wall model. We remark that the alternative wall model is not different from the wall model in Fluent, concerning the physical principles. The practical difference is that the alternative wall model is explicit.

2.4.3. Fluent wall treatment for LES

One of the options for LES is to use the no–slip treatment, which is also possible for the other models. This then simply means that the velocity is brought to zero at the walls. The no–slip approach requires a very fine grid near the walls and is therefore not justified in the study that we present here. The enhanced wall function approach of Fluent is unstable in LES. The implicit equation for u_τ (46) makes u_τ so dependent on itself that iterative procedures in LES do not converge. Therefore, in Fluent, another procedure is followed. In LES, when the mesh is fine enough, the wall shear stress is obtained from $\dfrac{u}{u_\tau} = \dfrac{\rho u_\tau y}{\mu}$. When a coarse mesh is used (as we do), the logarithmic law–of–the–wall, i.e. $\dfrac{u}{u_\tau} = \dfrac{1}{\kappa} \ln\left(\dfrac{E\rho u_\tau y}{\mu}\right)$, is used. The observation is that u_τ, and so τ_w^t, can be determined iteratively from these expressions. Further, no special action is taken to improve the determination of the velocity gradient in the production term of the dynamic kinetic energy SGS model for coarse grids.

2.4.4. An alternative wall model for LES

The determination of the wall shear stress can be made explicit.

We determine τ_w^t from (52). Since $\dfrac{uy}{\nu} = \dfrac{u}{u_\tau} \dfrac{yu_\tau}{\nu} = u^+ y^+$ we can plot $\dfrac{y^+}{u^+}$ for a range of $u^+ y^+$ values and fit a function to the graph. We obtain

$$\frac{y^+}{u^+} = f\left(u^+ y^+\right) = a + b\left(u^+ y^+\right)^c = a + b\left(\frac{uy}{\nu}\right)^c, \tag{56}$$

with a = 0.1, b = 0.02057 and c = 0.76879.

Since y^+ is sufficiently high ($> \approx 300$) no blending of the turbulent and viscous expressions for the wall shear stress is done.

The wall model is programmed with UDFs. We call this wall model our own wall model. We remark that the alternative wall model is not different from the wall model in Fluent concerning the physical principles. The practical difference is that the model is explicit.

2.4.5. Law–of–the–wall modified for roughness (Fluent)

In Fluent, the law–of–the–wall, modified for roughness has the form:

$$\frac{u_p u^*}{\tau_w / \rho} = \frac{1}{\kappa} \ln\left(E \frac{\rho u^*}{\mu} y_p \right) - \Delta B \tag{57}$$

where $u^* = C_\mu^{1/4} k^{1/2}$, and

$$\Delta B = \frac{1}{\kappa} \ln\left(f_r \right), \tag{58}$$

where f_r is a roughness function that determines the shift of the intercept. Since ΔB depends on the type and size of the roughness, no universal roughness function exists that is valid for all types of roughness. Often, a correlation of ΔB with the non–dimensional roughness height k_S^+ is adopted:

$$\Delta B = f\left(k_S^+ \right). \tag{59}$$

In this expression, $k_S^+ = \frac{\rho u^*}{\mu} k_S$, with k_S the physical roughness length.

In Fluent, the whole roughness regime is subdivided into three subregimes: the hydro–dynamically smooth regime ($k_S^+ \leq 2.25$), the transitional regime ($2.25 < k_S^+ \leq 90$) and the fully rough regime ($k_S^+ > 90$). In each regime, different formulas, proposed by Cebeci and Bradshaw (1977), are used to compute ΔB.

Hydrodynamically smooth regime ($k_S^+ \leq 2.25$):

$$\Delta B = 0 \tag{60}$$

Transitional regime ($2.25 < k_S^+ \leq 90$):

$$\Delta B = \frac{1}{\kappa} \left[\frac{k_S^+ - 2.25}{87.75} + C_S k_S^+ \right] \times \sin\left\{ 0.4258 \left(\ln\left(k_S^+ \right) - 0.811 \right) \right\} \tag{61}$$

Fully rough regime ($k_S^+ > 90$):

$$\Delta B = \frac{1}{\kappa} \ln\left(1 + C_S k_S^+ \right) \tag{62}$$

In these expressions, C_S is a roughness factor which takes into account the type of roughness. The default value is 0.5.

3. FLOW AROUND A SURFACE MOUNTED CUBE PLACED IN FULLY DEVELOPED CHANNEL FLOW

3.1. Computational domain

The geometry consists of a cube placed in a channel. The cube height H is 4 cm. The channel height is 2 times the cube height. The front side of the cube is a distance of 3 times the cube height from the inlet of the channel. The channel exit is 6 cube heights downstream of the leeward side of the cube. The side walls of the channel are at a distance of 3 cube heights left and right of the cube. A side view is given in figure 2. The flow direction is normal to the cube front face. Coordinates are measured in cm.
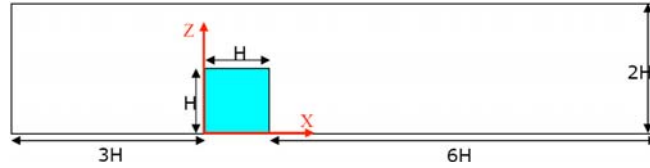
Figure 2: Cube in channel. Side view of the geometry.

The blockage ratio of the cube in the channel is about 7%. We also performed some of the simulations in a larger domain with channel width 11H, upstream length 5H and downstream length 15H, so that the blockage ratio becomes about 4.5%. We have compared results on the larger domain to results on the smaller domain to prove that the results on the smaller domain are almost not affected by the blockage ratio.

3.2. Computational grid

The mesh consists of a little more than 300.000 cells. On the cube itself, the cell distribution is 20 cells in X and Y directions, 25 in the Z direction. 25 cells are situated upstream of the cube and 50 cells downstream of the cube. Near the cube the first adjacent cell centre is at a distance of 4.6×10^{-2} cm from the cube walls (1.15 % of cube height).The maximum expansion ratio is 1.11. A top view of the mesh is given in figure 3.

For the larger domain, the grid has twice the number of cells. The maximum expansion ratio has been kept the same, but the lateral expansion ratio of the grid is bigger.
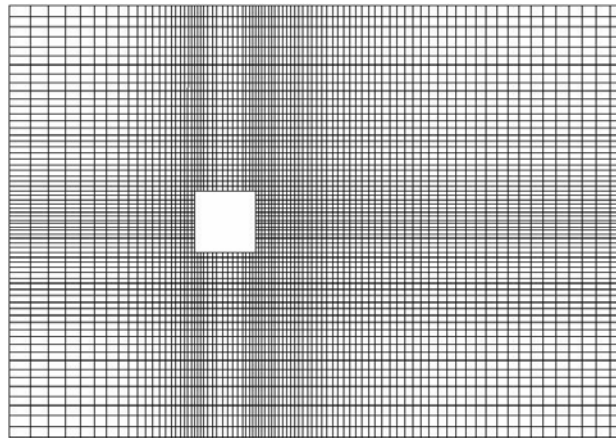
Figure 3: Cube in channel. Top view of the mesh (small domain).

3.3. Simulation settings

The Reynolds number of the flow, based on the cube height H and bulk velocity U_b, is Re = 4.10^4. We assume the air density as being 1 kg/m^3, the bulk velocity U_b as 10 m/s and the molecular viscosity as 10^{-5} kg/ms.

At the inlet of the channel we assume a fully developed turbulent velocity profile. To obtain such a profile we have performed a RANS simulation with the standard k–ε model and enhanced wall treatment of a turbulent channel flow on the same grid but without the cube placed in it and with periodic inlet and outlet.

Turbulence in the upstream flow is specified with profiles for k and ε. For the RANS simulations, these profiles for k and ε are again taken from the turbulent periodic channel flow simulation. For the LES, the information on k and ε is used to generate resolved fluctuations at the inlet with the vortex method (Mathey et al., 2006). For the hybrid RANS/LES, the length scale of the modelled turbulence is taken at the inlet as $\ell_{des} = \min\left(\ell_{rke}, \ell_{les}\right)$, with $\ell_{rke} = k^{3/2}/\varepsilon$ and $\ell_{les} = C_{des}\Delta$. The sub–grid turbulent kinetic energy is computed from $k_{sub} = \left(\varepsilon\ell_{des}\right)^{2/3}$. With the version of Fluent that we have used, it was not possible to simultaneously impose resolved fluctuations at the inlet in a hybrid RANS/LES. This means that in the hybrid simulations, we only take into account the small scale turbulence (sub–grid turbulence) in the incoming flow.

The left and right side walls of the channel are symmetry walls, while the channel outlet is an outflow boundary. The momentum equations and k, ε and ω equations are discretized with a second order upwind scheme for the RANS and the hybrid models, while the bounded central difference scheme is used in the LES for the momentum equations. The pressure on faces is obtained with second order accuracy as the mean of linearly reconstructed values on both sides of the face. The pressure–velocity coupling is done with the SIMPLE algorithm. The time stepping is the standard 4–stage low–storage Runge–Kutta scheme.

In all simulations the velocity is monitored in a point in the reattachment region behind the cube. We took this point at (10; 0; 0.5), with x = 0 being at the front of the cube. The monitoring point is in the most unsteady part of the flow domain. For steady simulations, we stopped the calculations when the velocity at the monitoring point reached a constant value. For the unsteady simulations we used a time step of 10^{-3}s. This time step ensures a CFL number of approximately 1. During every time step, iterations were done until the residuals (for velocity and the other turbulent quantities) dropped below 5.10^{-4}. In the unsteady simulations, we started from a steady solution and allowed the flow to develop for a number of time steps. We took at least 10 through flow times in order to be sure to obtain sufficient statistical convergence. Then, the averaging was enabled and iterations continued until the mean velocity at the monitoring point reached a near constant value. For RANS, we performed steady and unsteady simulations, but we did not see any difference between the results. So, hereafter, we only report results from steady RANS computations.

Figure 4 shows the evolution of the turbulent kinetic energy for some of the simulations on the basic domain. Profiles are shown at 2 locations: at the inlet and at X/H = –2. For the simulation with the standard RANS k–ε model, the profile of the turbulent kinetic energy remains almost unchanged in the flow approaching the cube. The reason is that the inlet profiles of velocity and turbulent quantities are the fully developed profiles for this model in an empty channel. For the hybrid simulations, the profile of the turbulent kinetic energy adjusts somewhat since the inlet profiles are not equilibrium profiles for these models. Further, there is also some influence from the obstruction by the cube. The results show that, up to some small adjustments, the inlet turbulent kinetic energy is advected towards the cube.
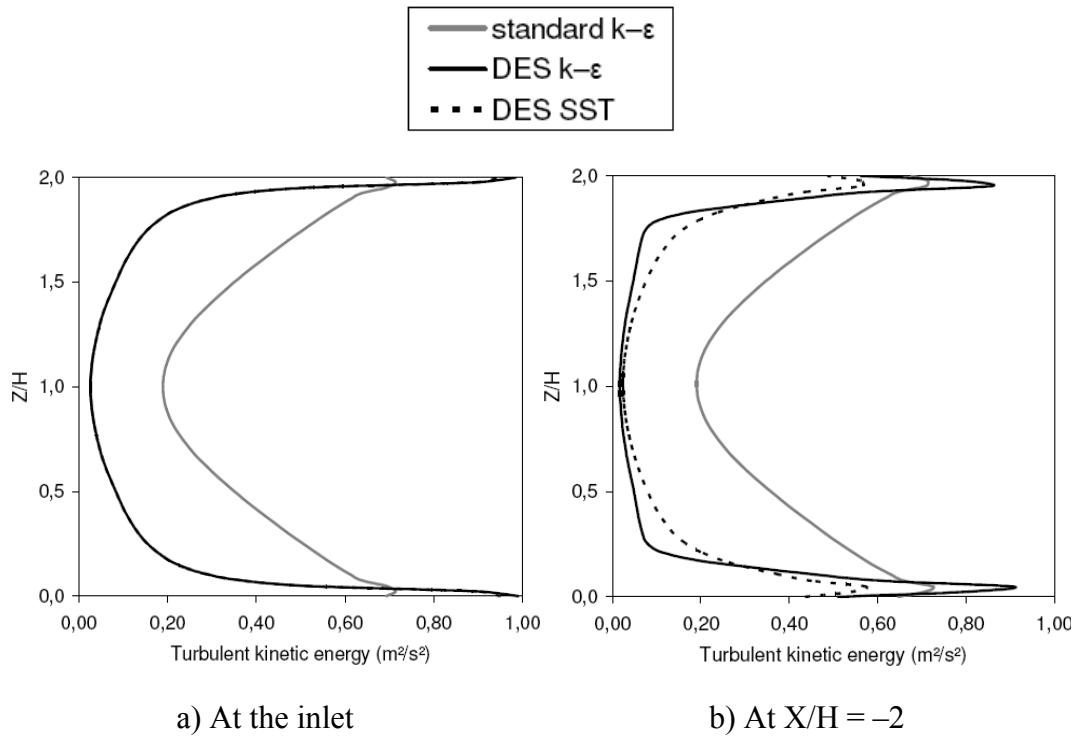
a) At the inlet   b) At X/H = –2

Figure 4: Evolution of the inflow turbulent kinetic energy for the RANS k–ε simulation and for two hybrid simulations.

3.4. Experimental data

Martinuzzi et al. (1993) investigated the flow field around surface–mounted, prismatic obstacles with different dimensions. The experimental data obtained from the measurements include the three components of the mean velocity at several upstream and downstream positions. All data have been added to the Journal of Fluids Engineering Data Bank.

Velocity profiles at the inlet and at the position X/H = –2, compared to the experimental profiles, are shown in figure 5 for some of the simulations on the basic domain and on the larger domain. There is almost no difference between the profiles obtained on the basic domain and on the enlarged domain. The correspondence with the experimental profiles is very good.

a) At the inlet

b) At X/H = –2
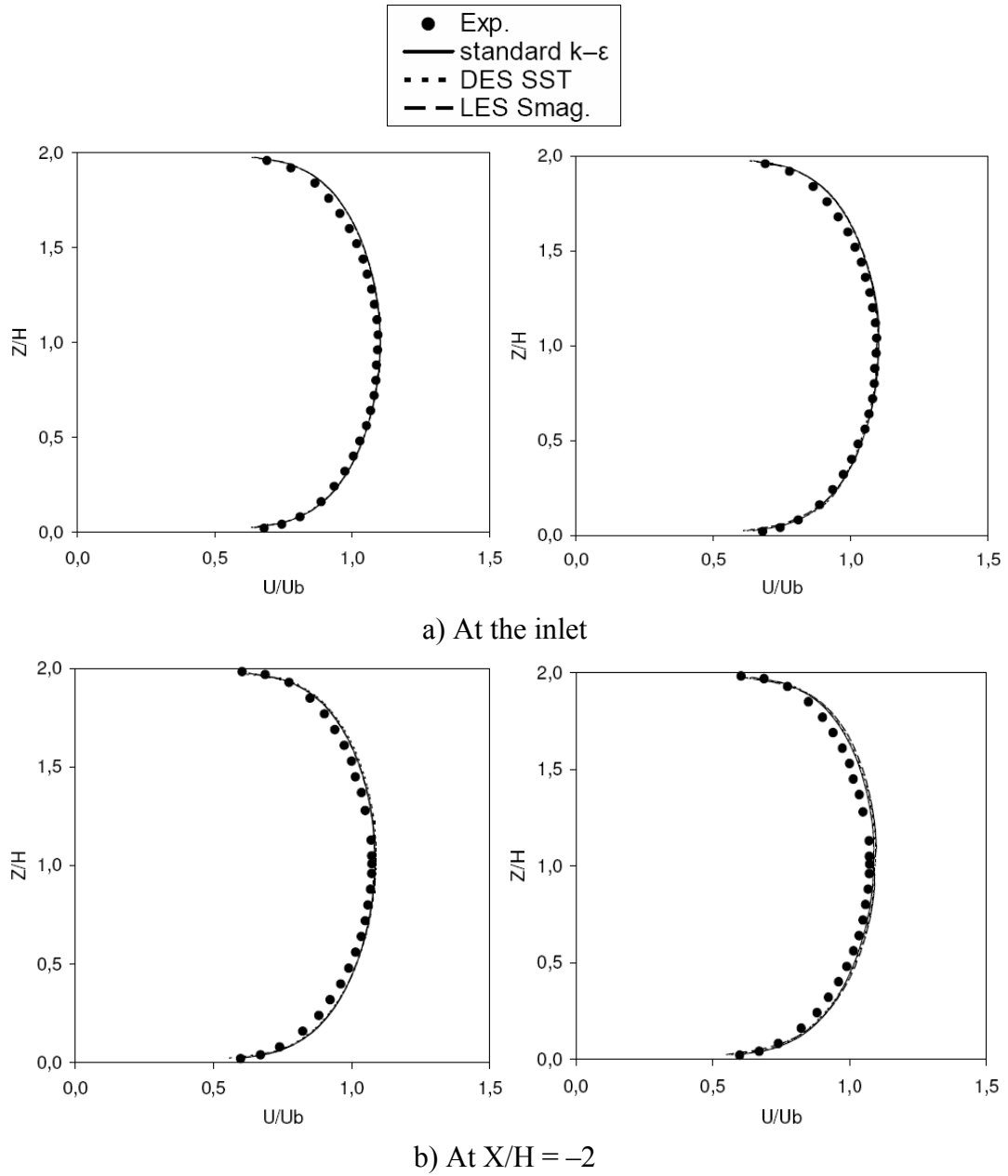
Figure 5: Evolution of the velocity profile. Left: large domain; right: basic domain.

3.5. Results

We compare mean streamwise velocity profiles at four locations in the symmetry plane (see figure 6). The focus is on the region in the immediate vicinity of the cube.
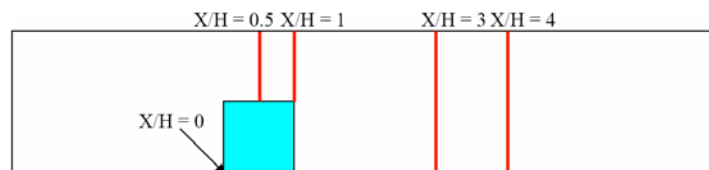
Figure 6: Cube in channel. Locations in the symmetry plane for velocity profile comparison.

3.5.1. RANS

In figure 7, mean velocity profiles at several locations are presented for the RANS–simulations. The plus signs represent the experimental data. The simulations have been carried out with the enhanced wall treatment. The RANS k–ε result differs very much from the experimental results. The results of the RANS SST k–ω model are nearer to the experiments at the top of the cube, but differ more in the wake of the cube. However, also at the top of the cube, the form of the predicted recirculation zone by the SST k–ω differs considerably from the experimental form. The results of the RANS models are comparable to the results obtained by Rodi (1997) on a coarser grid (about 100,000 cells) and a finer grid (about 750,000 cells) than we use. The general observation is that RANS underestimates the separation on the top of the cube and overestimates the length of the separation zone downstream of the cube. We illustrate the effect on the pressure distribution later.

3.5.2. Hybrid RANS/LES

Figure 8 shows mean velocity profiles obtained with the DES models of Fluent. The DES k–ε and DES k–ℓ simulations have been performed with the no–slip option, so without wall model, the DES SST k–ω with wall model. For the DES SST k–ω, the enhanced wall functions are implicitly active and cannot be deactivated. The hybrid RANS/LES results are good for the DES SST k–ω model, with wall model. The somewhat less performance of the hybrid k–ε and k–ℓ models is mainly due to absence of a wall model, as we demonstrate hereafter.

In figure 9, we present the results of the hybrid models when our own wall model, denoted by WM, is applied. Again, the results of the SST k–ω model are particularly good and are even somewhat better than obtained with the wall model of Fluent (figure 8). This small improvement has to be considered as a coincidence, since both wall models rely on the same physical principles. The other hybrid models also benefit from the introduction of a wall model, but the results are not as good as with the SST model. So, we conclude that the use of a wall model improves considerably the results of hybrid simulations.

3.5.3. LES and ILES

Figure 10 shows the velocity profiles obtained with the LES type of models with the wall model of Fluent. At the first two positions the results are very similar for all LES types. Minor differences occur at the positions aft of the cube. Even when the sub–grid scale model is omitted, the differences with the other simulations are very small. Compared to the results of the hybrid RANS/LES with wall model, the results of the LES types differ much more from the experiments. In particular, the difference with the experiments is big at the first position (X/H = 0.5). This means that the extent of the recirculation zone at the top of the cube is underpredicted. At the other positions, the results are somewhat less accurate than the hybrid RANS/LES results, but are quite acceptable. The basic reason why LES has difficulties in the area at the top of the cube is that the grid is much too coarse for a justified LES. As demonstrated by Rodi (1997), similar LES models as we use here lead to very accurate results, if the grid is finer and if a wall model is used. For the same case, Rodi used grids with approximately 1 million grid cells. The coarse grid that we use here gives an advantage to the hybrid simulations. This is the basic reason why the hybrid simulations give superior results. It is clearly more accurate to simulate a few cells in wall vicinity in RANS–mode than to bridge the wall region with a wall model.
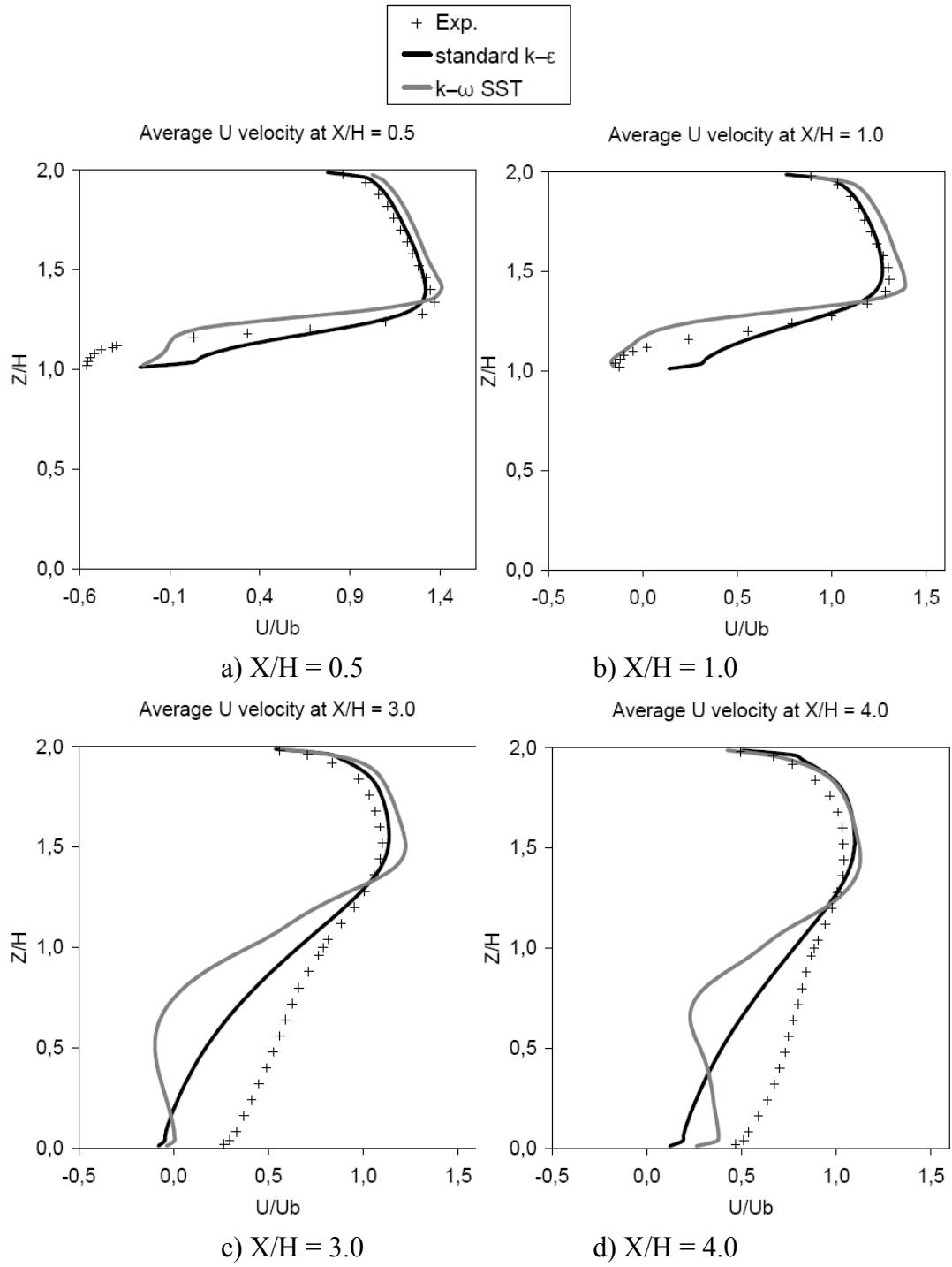
Figure 7: Cube in channel. Mean streamwise velocity in the symmetry plane at X/H = 0.5, 1.0, 3.0 and 4.0 for RANS simulations.
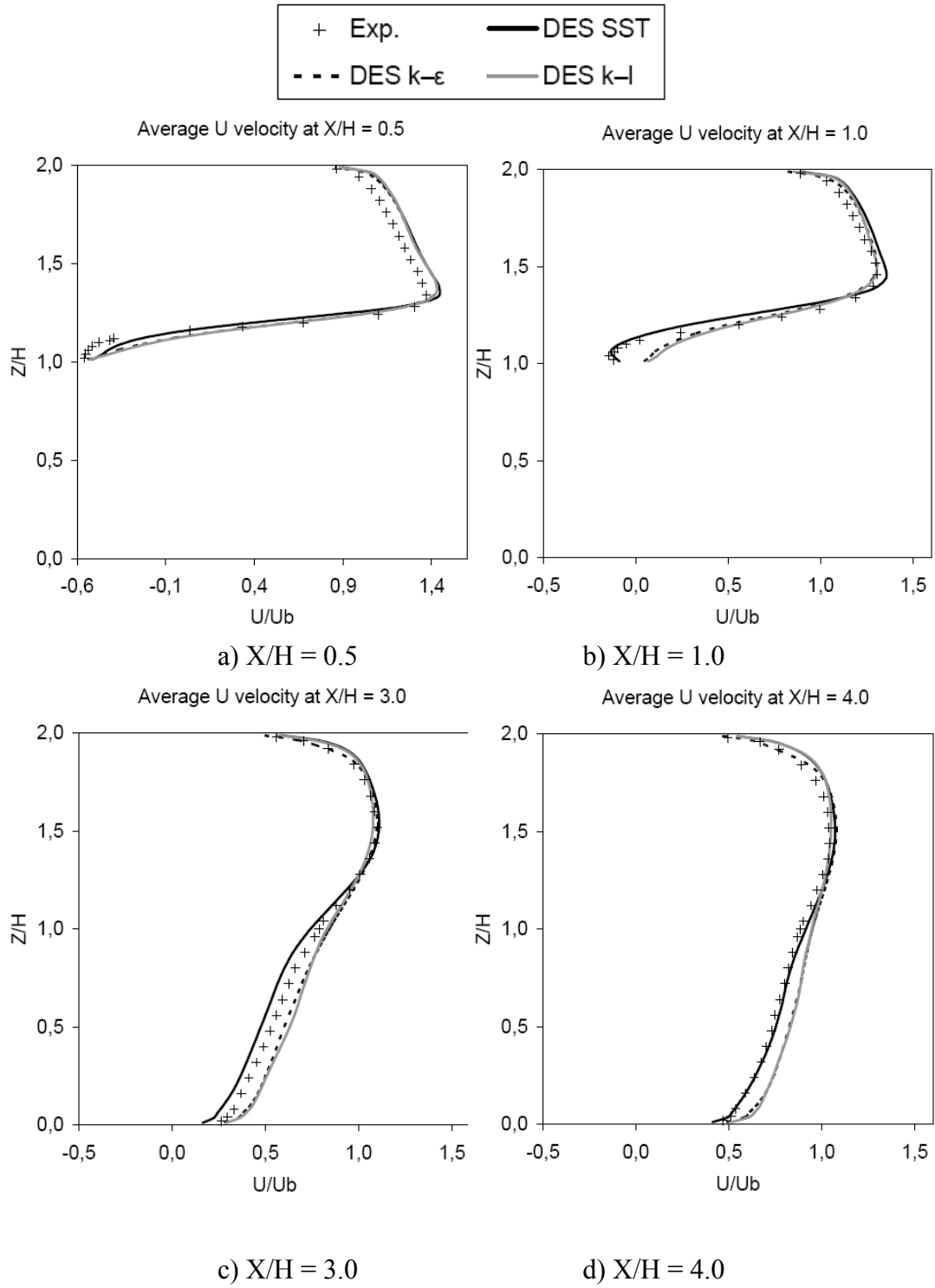
a) X/H = 0.5   b) X/H = 1.0

c) X/H = 3.0   d) X/H = 4.0

Figure 8: Cube in channel. Mean streamwise velocity in the symmetry plane at X/H = 0.5, 1.0, 3.0 and 4.0 for Hybrid simulations. DES k–ε and DES k–ℓ without wall model. DES SST k–ω with wall model of Fluent.
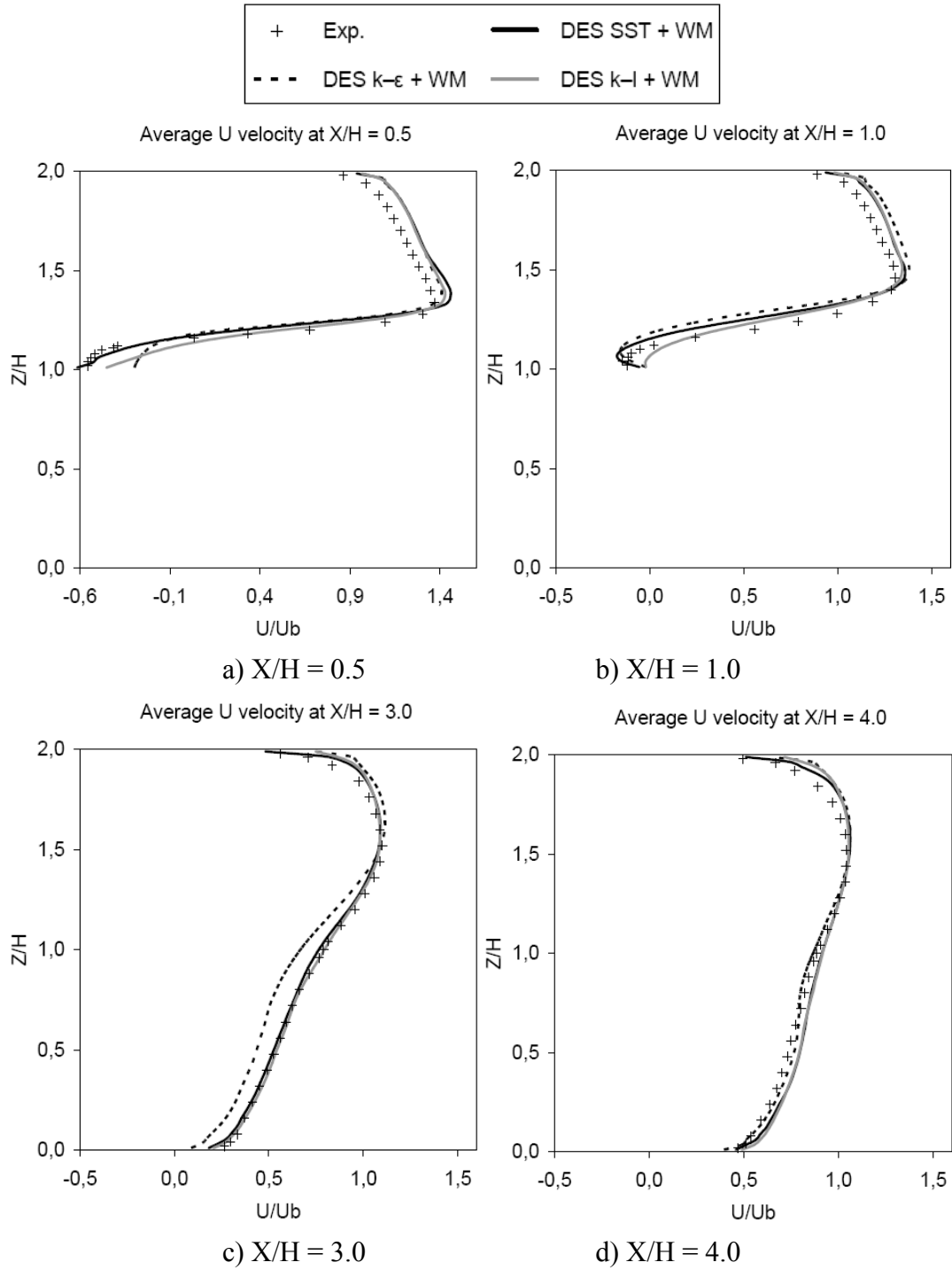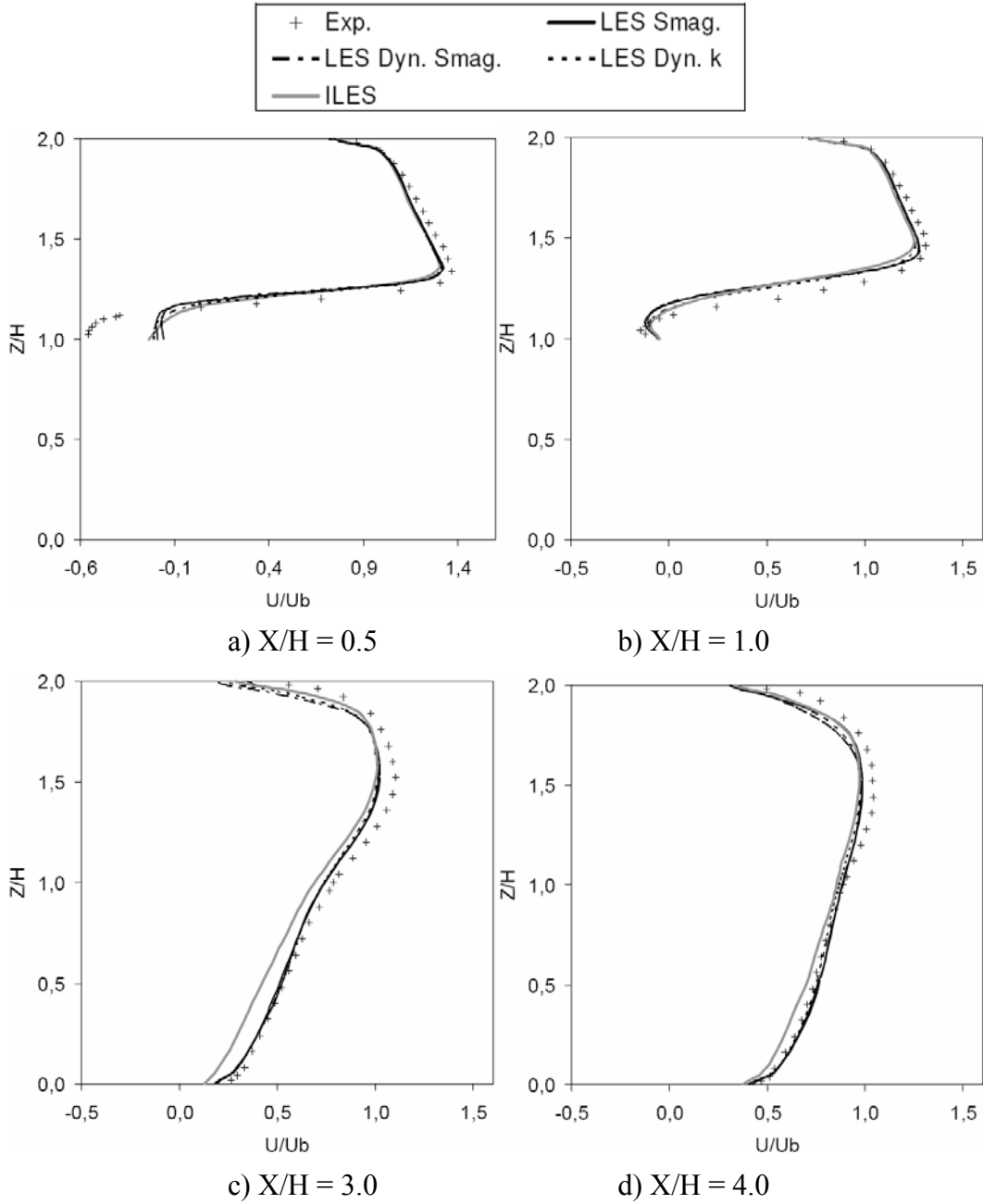
a) X/H = 0.5   b) X/H = 1.0

c) X/H = 3.0   d) X/H = 4.0

Figure 9: Cube in channel. Mean streamwise velocity in the symmetry plane at X/H = 0.5, 1.0, 3.0 and 4.0 for hybrid simulations with own WM.

Figure 10: Cube in channel. Mean streamwise velocity in the symmetry plane at X/H = 0.5, 1.0, 3.0 and 4.0 for LES and ILES with the wall model of Fluent.

3.5.4. Magnitude of error on the velocity

For the best performing models, like the hybrid models, especially the DES SST, the general correspondence between the predicted velocity profiles and the experimental velocity profiles is visually very good (figure 9) at all stations. However, quantitative differences may be quite high at some positions, especially in the recirculation zone at the top of the cube. The maximum velocity difference is there in the order of 20 % of the free stream velocity. So, it is clear that a quantitative comparison is difficult to make based on velocity magnitude differences. The objective of our study is the pressure distribution prediction on the cube surface. However, there are no experimental data on the pressure distribution. Therefore, we

will come back to the aspect of quantification of the difference between predictions and experiments in section 4 on the simulation of a cubical building in the atmospheric boundary layer.

3.5.5. Pressure distribution prediction

Figure 11 shows the pressure coefficient profiles on a vertical (mid plane) and a horizontal section (mid plane) of the cube. We do not have experimental results, but from the good quality obtained for velocity profiles with the DES SST, we may assume that the pressure distributions with this model are of good quality. The RANS predictions deviate a lot from the other predictions and the profiles obtained by the two types are very different. The observation is that the somewhat better quality of the velocity profiles at the top of the cube by the k–ω SST model (figure 7), does not lead to a significantly better prediction of the mean pressure distribution in this area. The hybrid and ILES results are very similar, except at the front of the top and the front of the side walls. These differences are caused by the underestimation of the intensity of the back flow in the recirculation zones by the ILES (figure 10). However, the ILES prediction of the pressure distribution still can be considered as of good quality, when compared to the RANS results.

a) Vertical section   b) Horizontal section
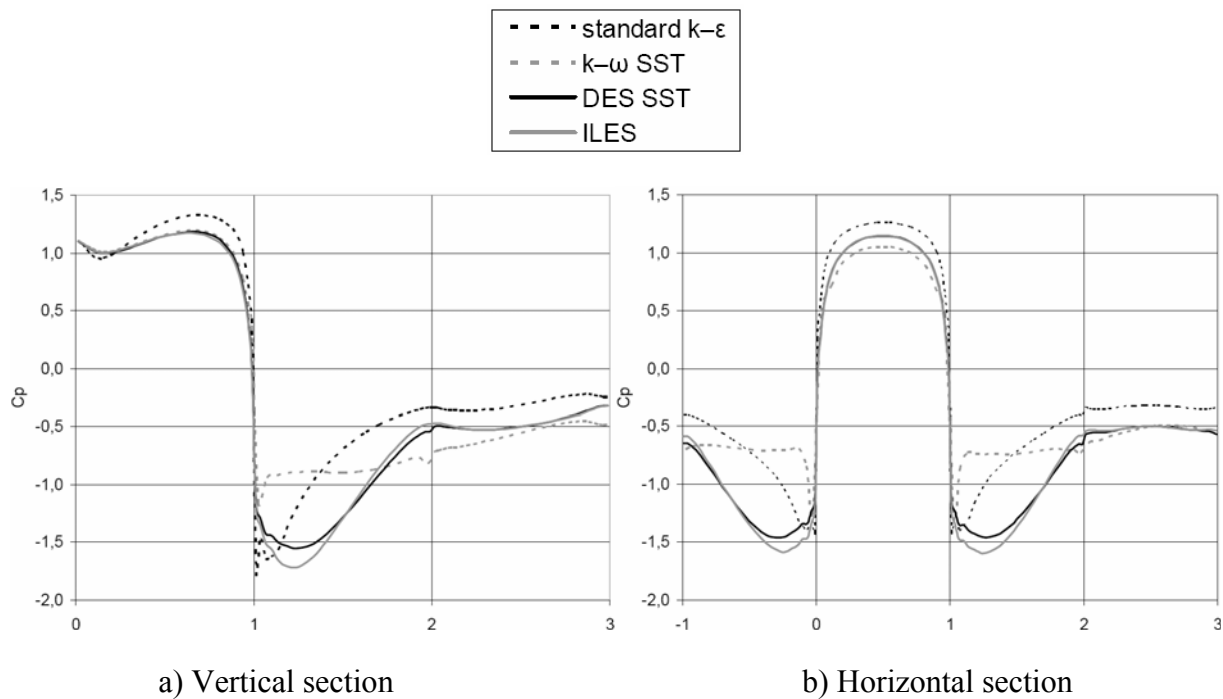
Figure 11: Cube in channel. Pressure coefficient profiles on vertical and horizontal sections. RANS, hybrid and ILES results. The numbers −1 to 3 represent the different faces of the building: from −1 to 0: side face, 0 to 1: front face, 1 to 2: top or side face and 2 to 3: back face.

3.6. Sensitivity to the domain extension

Figure 12 shows hybrid simulation (DES k –ε without wall model, DES SST with wall model) results for the velocity profiles at x/H = 0.5 and X/H = 4.0, for the basic domain and for the larger domain. There is almost no difference in the results on both grids for the k–ε model, while some differences can be observed for the DES SST predictions. At the top of the cube, there is very little influence of the domain extension. So, as the near field of the flow around the cube is the most important for the prediction of the mean pressure on the building surface, the use of the basic grid in our study is justified.
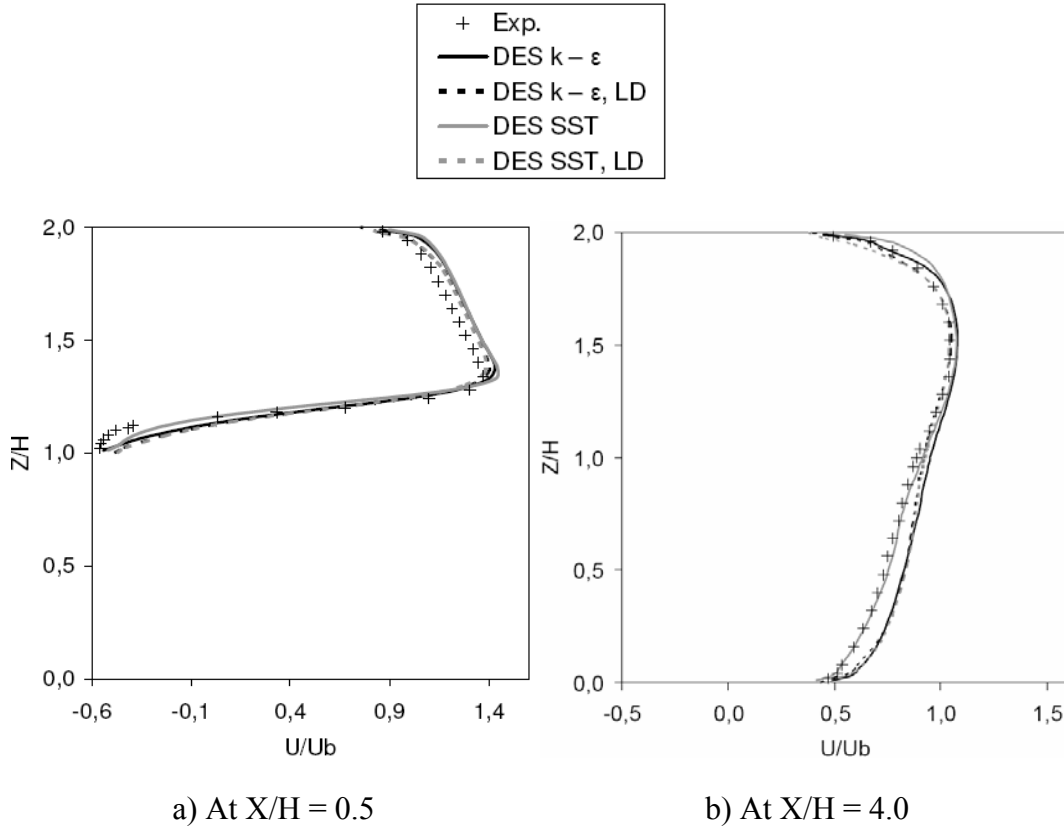
a) At X/H = 0.5   b) At X/H = 4.0

Figure 12: Comparison of mean velocity at two locations on the basic domain and the large domain (LD) for hybrid simulations. DES k–ε without wall model, DES SST with wall model.

3.7. Best model for low Reynolds number

The conclusion from the results in figures 7 to 11 is that there is an advantage in using a hybrid formulation. RANS is clearly erroneous due to the impossibility to represent the unsteadiness of the large vortex structures shed by the cube. LES leads to an underestimation of the length of the recirculation zone at the top of the cube. The lower performance of LES has to do with the resolution in wall vicinity. The y^+ value at the centre of the first cell on the cube walls varies from 7 to 115. This value is much too big for accurate representation of the near wall zone by LES, even when a wall model is used. We remark that the y^+ value is also too big for RANS simulation and hybrid RANS/LES without wall model. This explains why the hybrid results benefit from the introduction of a wall model.

The conclusion from the comparison is that the DES SST k–ω model with wall model gives the best results.

In order to further illustrate why hybrid RANS/LES is optimal for the simulation at low Reynolds number, we show in figure 13, the RANS and LES zones for an instantaneous flow field in the symmetry plane of the channel. RANS is applied in the immediate vicinity of the walls and LES in the core of the flow. This figure explains why the hybrid simulation is much more qualitative than the RANS simulation, since the core of the flow is represented in LES, so that the unsteadiness of the vortices around the cube can be captured. The figure also explains why the hybrid simulation is more qualitative than the LES, since in wall vicinity, the viscous behaviour is much better simulated by RANS, due to the coarse grid near walls.
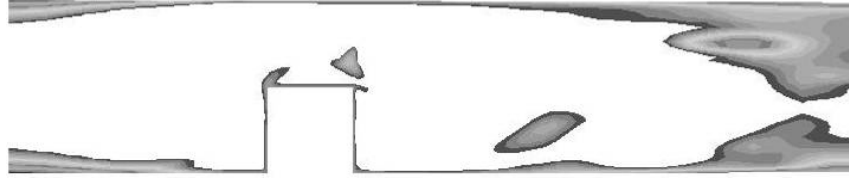
Figure 13: RANS (grey) and LES (white) zones in the symmetry plane for DES SST simulation.

4. FLOW AROUND A CUBICAL BUILDING IN AN ATMOSPHERIC BOUNDARY LAYER (ABL)

4.1. Computational domain

The computational domain extends 10H (H is building height) in streamwise direction, 7H in lateral direction and 5H in height direction. The building is placed at a distance 3H from the inlet of the domain. The side walls are at a distance 3H from the building. The cube height is 6 m. The coordinate system is as in the previous case. Coordinates are in m.

Some of the simulations were repeated on a larger domain with the same dimensions as described in section 3.1. However, we did not observe significant differences between the results on the larger domain and the basic domain. Therefore, we will present the results from the simulations on the basic domain described above, but we will show some results on the larger domain for comparison.

4.2. Computational grids

In order to avoid large computational cost, a typical RANS grid (mesh A), sufficiently fine for RANS calculations in steady flow and a second grid, mesh B, better adapted to LES, are used.

Both meshes are structured. Mesh A has a little more than 800.000 cells. The cell distribution on the building walls is 30 cells in all directions, with the first near–wall cell centre at a distance of 0.45cm (the cube height H is 6m). There are 35 cells upstream and in the lateral directions, 45 cells in the Z direction (starting at the top of the cube) and 55 cells downstream. The maximum expansion ratio for mesh A is 1.3. Figure 14 gives a view of the mesh.
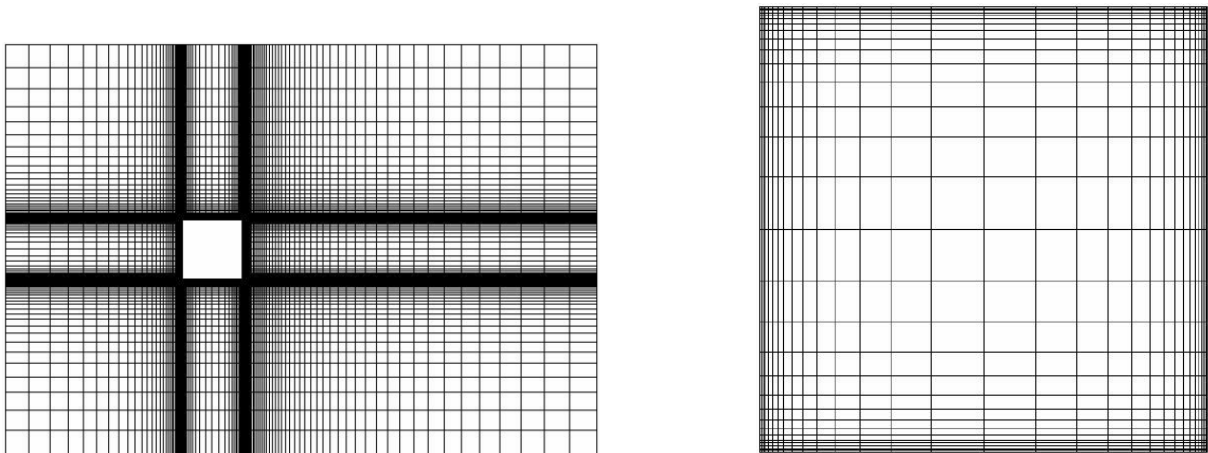

Figure 14: Cubical building in ABL. View of mesh A and cell distribution on building top wall.

For mesh B, we started from a coarse mesh and refined it twice in the building vicinity. A refinement consists in splitting a cell into 8 cells with equal size. After two refinements, the grid has approximately 1.2 million cells. Mesh B was refined a first time in the hexahedral region defined by the diagonal with begin point (–1.4; –6; 0) and end point (9; 6; 10) and a second time in the hexahedral region defined by the diagonal with begin point (–0.5; –4; 0) and end point (7; 4; 7). The difference between mesh A and mesh B is that the latter has n a lot more cells (a factor of 12) on the building surfaces and is thus better suited to resolve smaller scales. Figure 15 gives a view of the mesh in the vicinity of the cube.
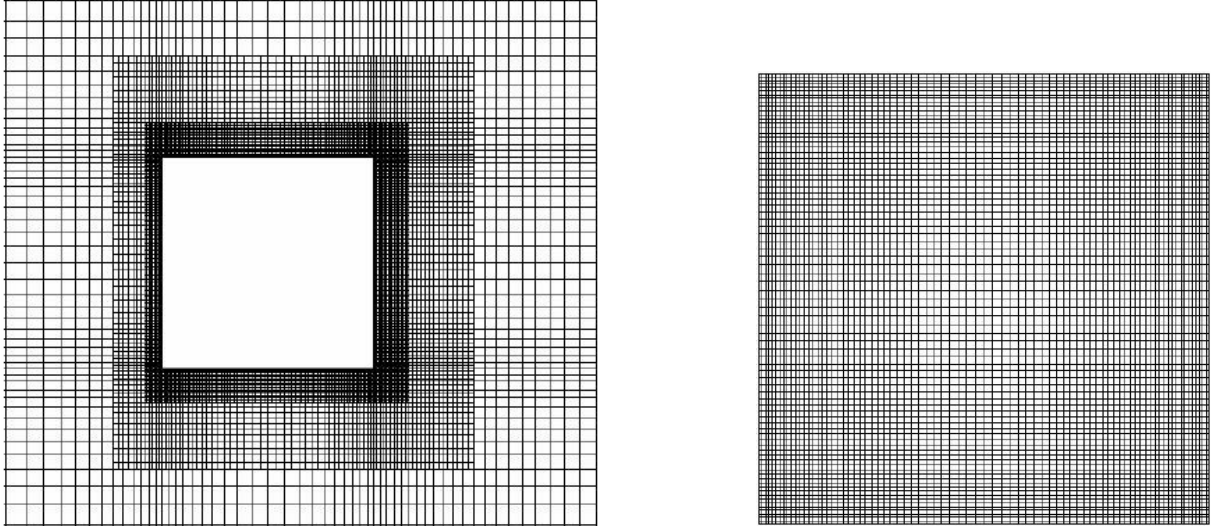
Figure 15: Cubical building in ABL. Close–up of mesh B and cell distribution on building top wall.

4.3. Turbulence models used

We have performed simulations with three types of models.

Steady state RANS models

- The standard k–ε model

- The k–ω SST model

Hybrid RANS/LES model

- The DES SST model

We only use one hybrid model since, in section 3, the DES SST model gave the best results.

LES and ILES models

- The Smagorinsky–Lilly model ($C_s = 0.1$)

- ILES (Implicit LES): no SGS model ($C_s = 0.0$)

4.4. Experimental data

From the field measurements of Richards et al. (2001) we have the properties of the approaching flow: velocities and turbulence intensities. We also have pressure coefficient profiles on a vertical and a horizontal section on the building.

4.5. Simulation settings

The Reynolds number, based on cube height H and velocity of the approaching flow at cube height, is Re $= 4.10^6$.

At the inlet of the channel we assume a logarithmic velocity profile:

$$U(z) = 1.194 \ln(z) + 7.38, \tag{63}$$

where z is the spanwise coordinate. This formula was derived from the available data of the approaching flow in the experiment.

In the RANS simulations, the turbulence in the upstream flow is specified with profiles for k and ε or k and ω. The profile for k is derived from the experimental data. The length scale is taken in the classical way by $l = 2.5z$, where z is the height above the ground. ε and ω are computed from

$$\varepsilon = \frac{k^{3/2}}{\ell} \text{ and } \omega = \frac{\varepsilon}{0.09k}. \tag{64}$$

For the hybrid RANS/LES, a procedure similar as described in section 3.3 is used. $\ell_{des} = \min(\ell_{rke}, \ell_{les})$, where here $\ell_{rke} = 2.5z$ and $\ell_{les} = C_{des}\Delta$. The sub–grid turbulent kinetic energy is computed from $k_{sub} = (\varepsilon \ell_{des})^{2/3} = k(\ell_{des}/2.5z)^{2/3}$.

For LES, fluctuations at the inlet are synthesised with the vortex method. No resolved fluctuations are generated in the hybrid RANS/LES.

The left and right side walls of the channel are symmetry walls, while the channel outlet and the top of the domain are pressure outlet boundaries. The discretization options are the same as for the cube in the channel (section 3.3). The monitoring point is taken in the recirculation zone behind the building (15; 0; 0.5).

A time step of 0.01s is used in the unsteady simulations. This time step ensures a CFL number of approximately 1. During every time step, iterations were carried out until the residuals for U, V, W and k and ε or ω dropped below 5.10^{-4}. In the unsteady simulations, we started from a steady solution and let the flow develop for a number of time steps (typically 10 through flow times). Then, the averaging was enabled and iterations continued until the mean velocity at the monitoring point reached a near constant value. The averaging time was always 2 minutes of simulation. This is approximately 10 through flow times.

The roughness in the experiments lies between 6 mm and 10 mm. In the LES simulations, no roughness was taken into account, since in Fluent it is not possible to specify roughness with these models. In the RANS and Hybrid simulations, roughness effects can be included by specifying the roughness height and the roughness constant. Since it is not meaningful to impose a roughness height larger than half of the near–wall cell height, the maximum possible value for the roughness height and roughness constant, i.e. 4.5 mm and 1 respectively, were applied.

Taking into account roughness does not have much influence on the velocity or pressure profiles, as we will demonstrate later. However, roughness has some effect on the approach flow velocity profile. Figure 16 shows the velocity profile at position X/H=−2 in the lowest part of the domain (< 2m) for rough and smooth conditions.

The velocity profile is only affected very near to the ground, approximately in the lowest 40 cm. So, the roughness effect is very limited. Therefore, most simulations were done without roughness and we will show only a few results with roughness to demonstrate that the results are insensitive to roughness.
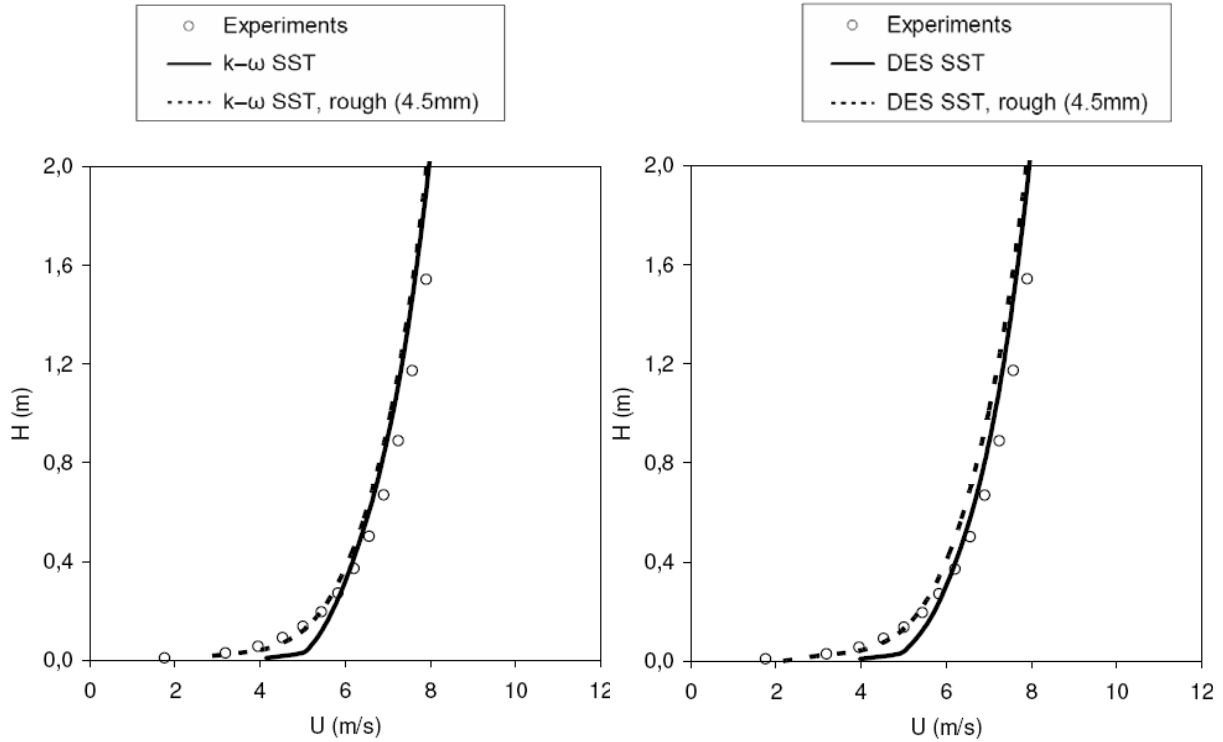
Figure16: Influence of roughness on the mean velocity profile at X/H = −2. Only the lower part of the domain (< 2m) is shown.

4.6. Results

The pressure coefficient is defined as the mean static pressure minus a reference pressure divided by the dynamic pressure at 10m height. The reference pressure is not specified in the experiments. We use pressure outlet boundaries at the top of the computational domain and at the outlet. We take the pressure imposed at these boundaries as the reference pressure.

4.6.1. Mesh A

The numbers −1 to 3 represent the different faces of the building: from −1 to 0: side face, 0 to 1: front face, 1 to 2: top or side face and 2 to 3: back.

RANS results

The pressure coefficient profiles on the vertical and horizontal sections are shown in figure 17 for the steady state RANS simulations. The steady state predictions are very poor at the top and the side walls of

the building. The best agreement with experimental data is at the front. The reason for this discrepancy is that the flow is highly unsteady. Since the RANS models give averaged results, the flow is represented too steady. The results of our RANS simulations are fully in accordance with the results reported by Richards and Hoxey (2006). For the vertical section, on the roof, results by Richards and Hoxey have been added for comparison.
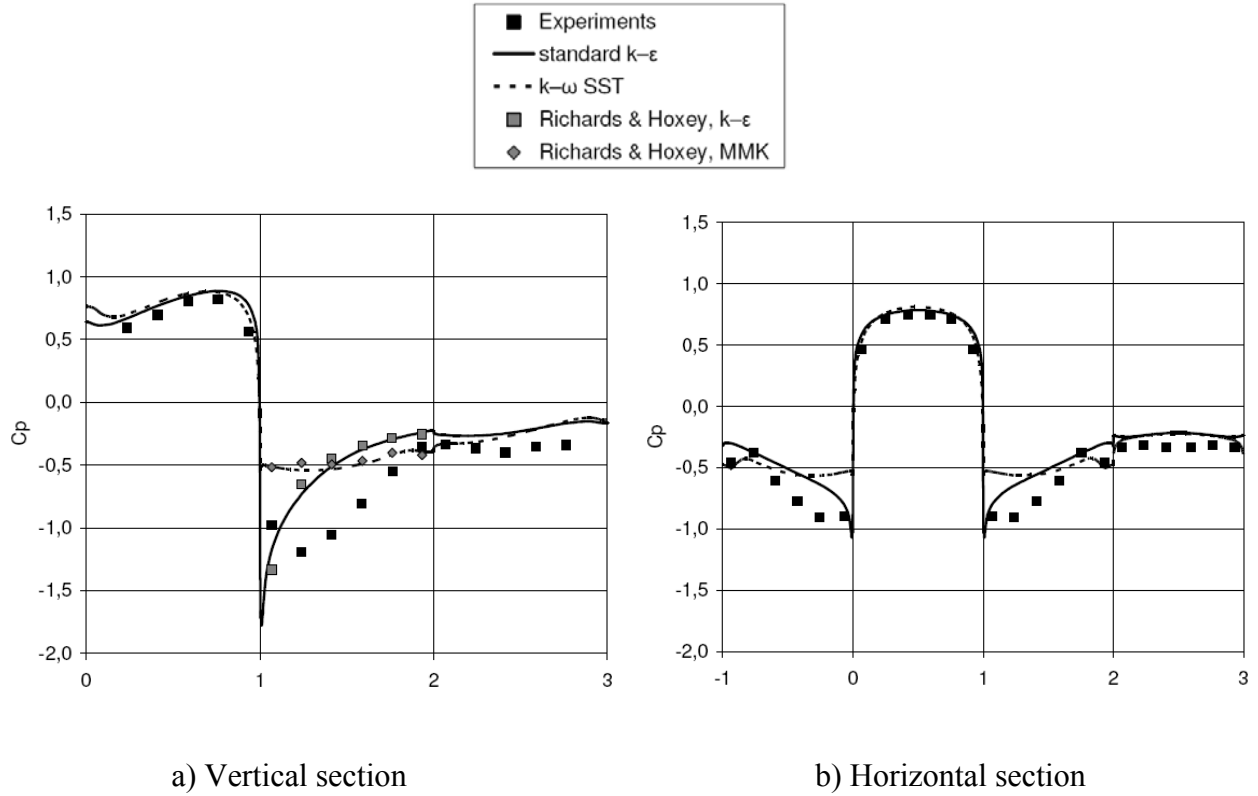

a) Vertical section   b) Horizontal section

Figure 17: Cubical building in ABL. Pressure coefficient profiles on the vertical and horizontal sections, RANS results on mesh A. Black squares are experiments. For the vertical section on the roof, grey squares represent results by the standard k–ε and grey diamonds represent results by the MMK k–ε model by Richards and Hoxey.

HYBRID simulation results

In figure 18, we show results for the DES SST model. We include the k–ω SST RANS results for comparison. The DES–SST results do not differ much from the steady state RANS predictions, except somewhat at the back. Again, the results are poor at the top and side walls.

a) Vertical section   b) Horizontal section
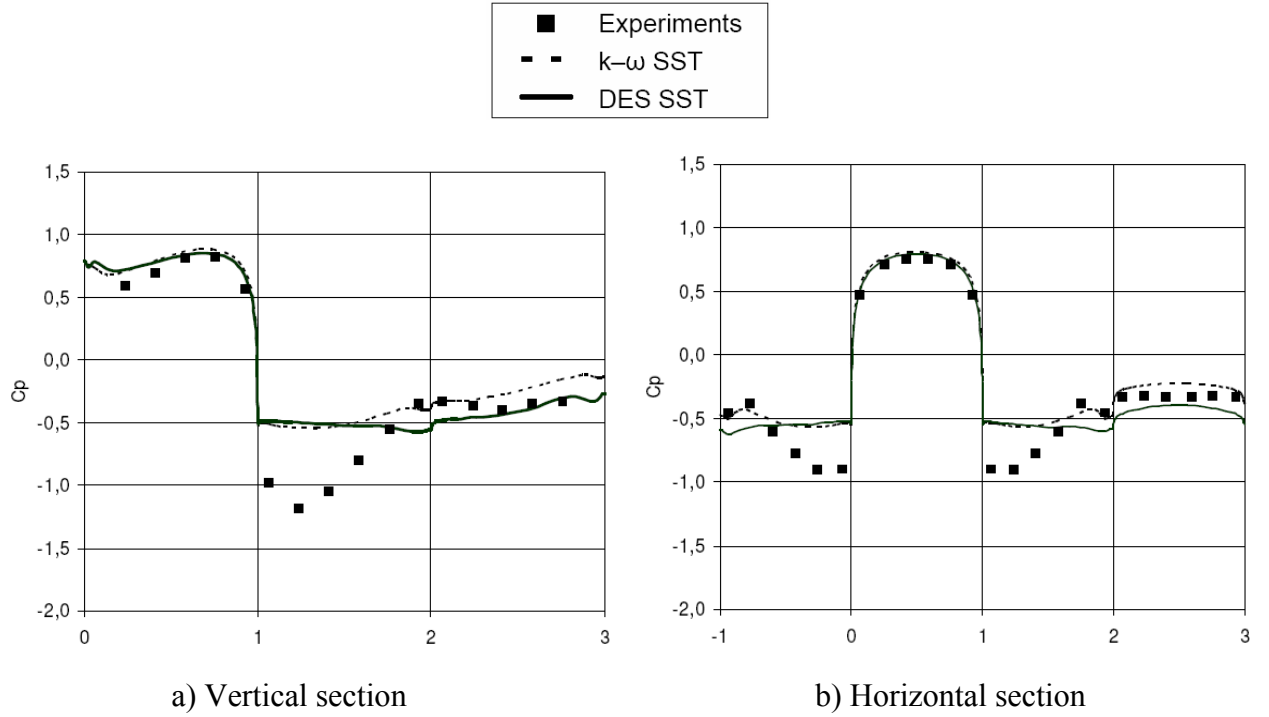
Figure 18: Cubical building in ABL. Pressure coefficient profiles on the vertical and horizontal sections, HYBRID results on mesh A, compared to RANS results. Black squares are experiments.

The poor results by the DES SST model contrast with the very good results that we obtained for low Reynolds number. In order to analyse the reason for this disappointing performance, we show an instantaneous picture of the RANS and LES zones in the symmetry plane in figure 19. It is obvious that the RANS zones are only present very close to walls and that the large surrounding of the building is simulated in LES. As such, this is wanted behaviour. Figure 20 shows the turbulent viscosity ratio in the symmetry plane. The white colour corresponds to the high values. Above the building and in the wake of the building the viscosity ratio is in the order of 5000 to 15000. This is very high and certainly much higher than what one would expect in an LES zone. Figure 21 shows the profile of the viscosity ratio for DES on the position X/H = 0.5 and the corresponding profiles for RANS and LES. The viscosity ratio for DES is lower than the viscosity ratio for RANS, but is, indeed, high in the vicinity of the building and much higher than the LES value. Apparently, in the hybrid simulation, the LES zone does not behave as a true LES zone, but more like a RANS zone. This means that the RANS model, which is modified by limiting the length scale in the destruction term of the equation for turbulent kinetic energy to allow it to function as a model for a sub–grid viscosity, does not fully reach this goal. This is due to the coarse grid that we use here. The y^+ values in the first cell at the cube top wall vary between 15 (near a separation point) to about 800. These values show that the grid is, indeed, very coarse. This means that, in the vicinity of the cube walls, the difference between the integral length scale of the turbulence and the grid size is not very significant. Hence, reduction of the length scale in the destruction term of the equation of turbulent kinetic energy to the grid size does not bring the length scale sufficiently down in the energy cascade. This implies that the modification of the RANS model does not reach the quality to serve as a well justified sub–grid model in LES. The situation is clearly much different from what we observed in section 3 for low Reynolds number. The coarseness of the grid has a similar effect in the flow above the cube. Again, due to the very coarse grid, the difference between the integral length scale of the turbulence and the grid size is not very large. So, for very coarse grids and high Reynolds number flows, hybrid RANS/LES models of DES–type are not justifiable.
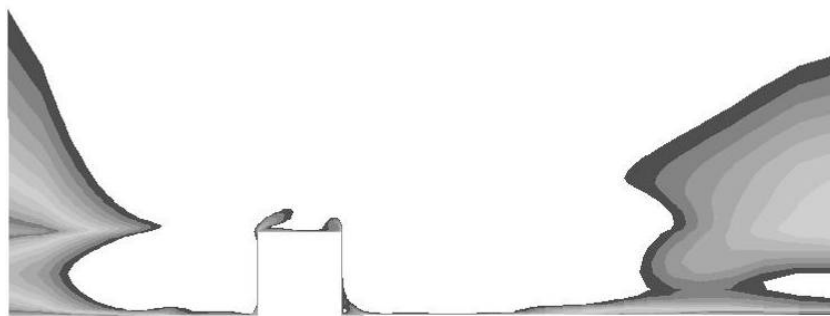
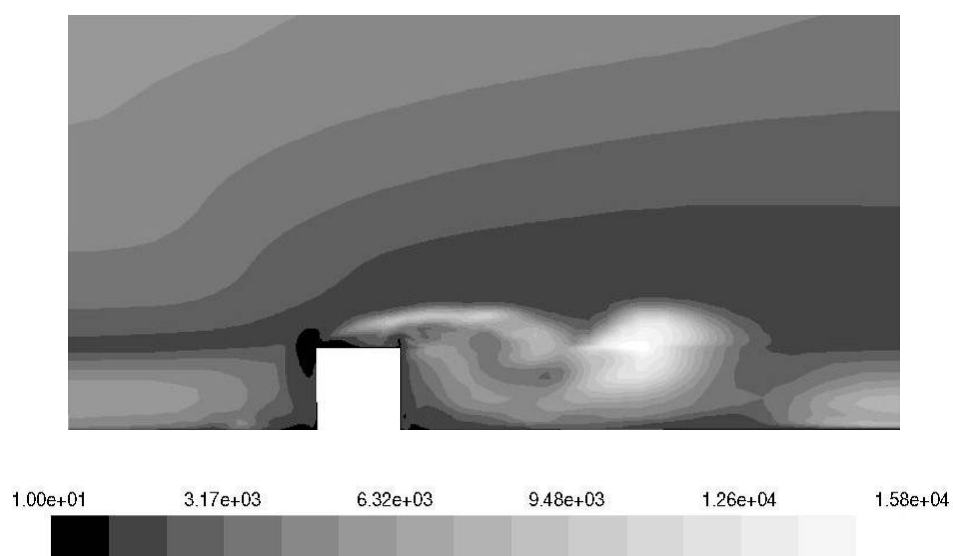Figure 19: RANS (grey) and LES (white) zones in the symmetry plane for the DES SST simulation.

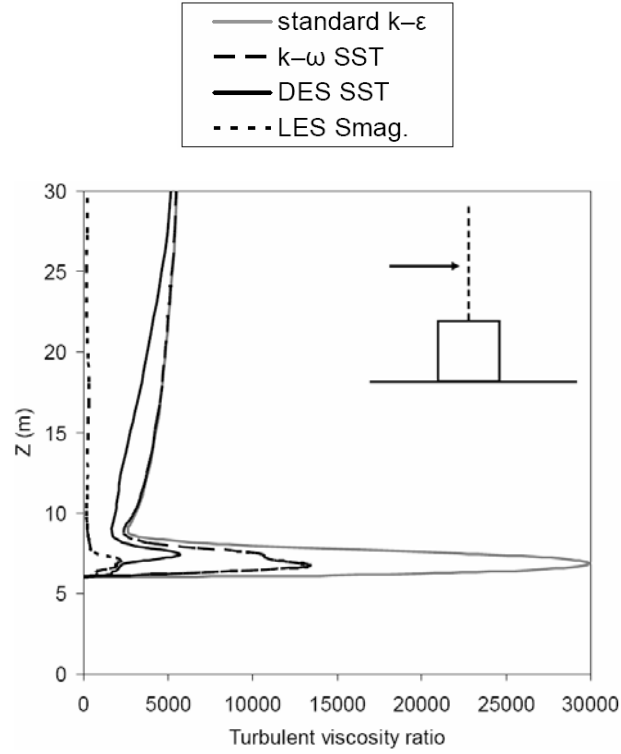Figure 20: Turbulent viscosity ratio in the symmetry plane for the DES SST simulation.

Figure 21: Turbulent viscosity ratio at X/H = 0.5 in the symmetry plane for the DES SST simulation, compared to the RANS results and LES (Smagorinsky–Lilly with C_S = 0.1) results.

LES and ILES results

We see on figure 22 that there is almost no difference between the LES and the ILES results, except at the front of the building (vertical section). This means that on the very coarse grid that we use, the SGS model has very little influence and that the sub–grid dissipation basically comes from the numerical scheme. There is also very little influence of the wall model. Results with our wall model (WM) are almost the same as with the wall model of Fluent. However, we have to admit that there is not much difference between the two wall models. They both use the logarithmic layer law, the Fluent version in implicit form and our own version in explicit form.

There is a strong agreement with experimental profiles at the front, on the top and at the back of the building. The predictions on the side walls follow the experimental profiles, but there is some deviation. Overall, it is remarkable that we can obtain such good correspondence between ILES results and experiments on a rather coarse grid, which is certainly not fine enough to resolve the small scales. This means that the flow is largely dominated by the large scale vortices shed by the building and that resolution of the precise way in which these break up into smaller segments is not very crucial to determine the mean pressure distribution.
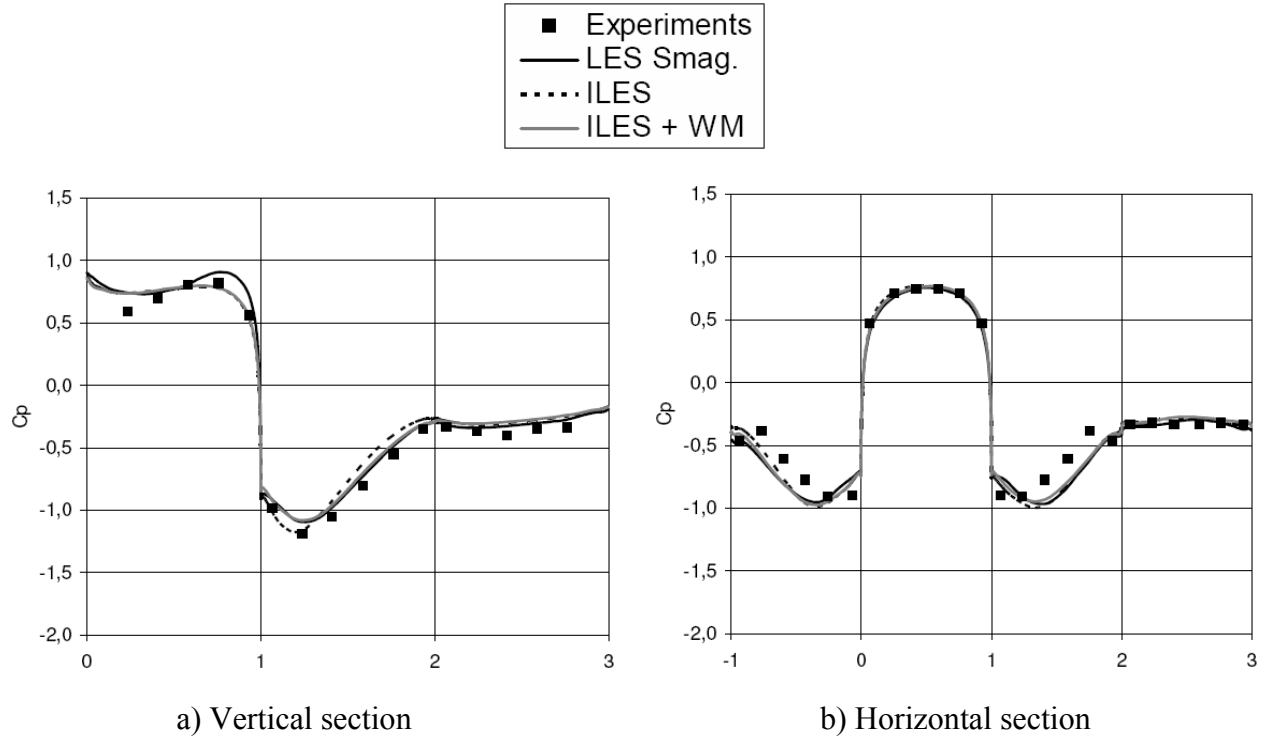
a) Vertical section   b) Horizontal section

Figure 22: Cubical building in ABL. Pressure coefficient profiles on the vertical and horizontal sections. LES and ILES results on mesh A.

4.6.2. Mesh B

All simulations are repeated on mesh B. Figure 23 shows the RANS and hybrid results, while the LES and ILES results are presented in figure 24. Again, the RANS and hybrid results are poor while the LES and ILES results are good.

The grid refinement does not seem to have a significant influence on the results (see results on mesh A in section 4.6.1). For the vertical section, the LES and ILES results of mesh A are somewhat better. For the horizontal section, the LES and ILES results on mesh B are the best.

We observe that the overall quality of the predictions is not really better on mesh B than on mesh A. This means that both meshes are much too coarse to resolve enough in wall vicinity. The differences in the results are due to the different mesh size in wall vicinity, but there is no conclusion on the best grid strategy. The observation is that any LES formulation gives good results, taking into account the very coarse grids used.
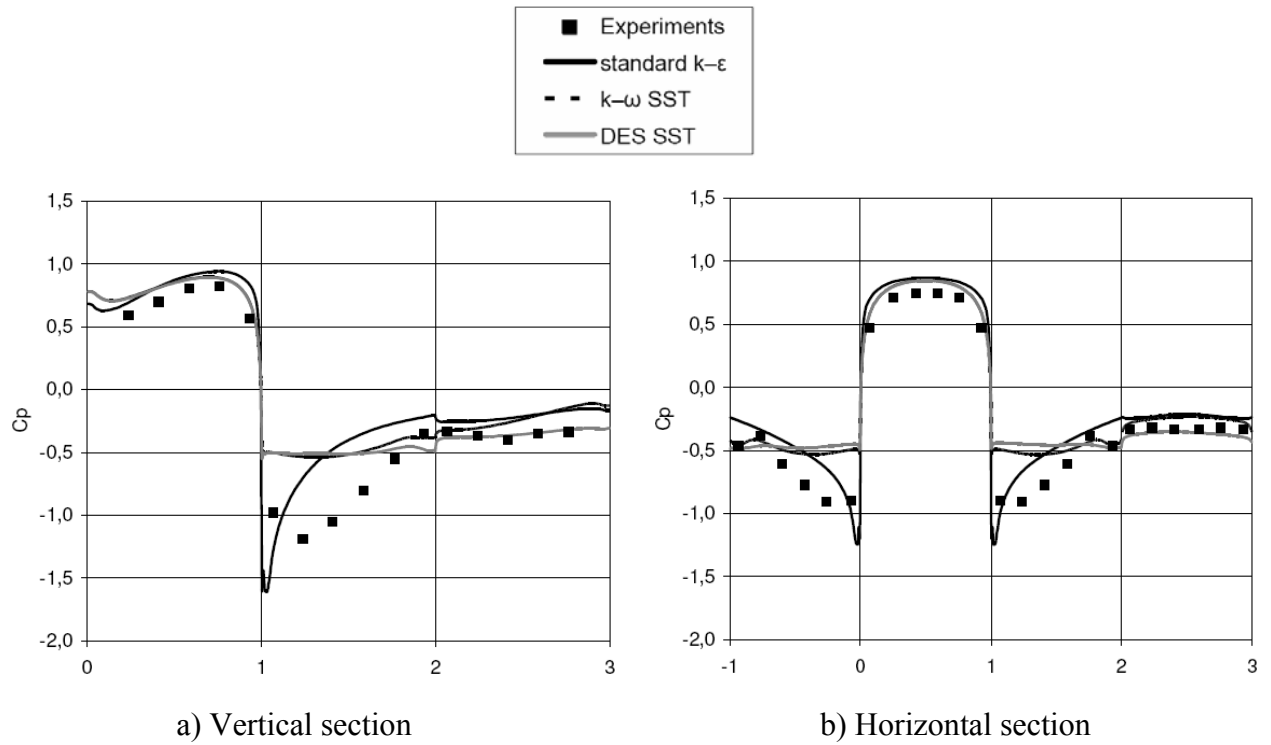
Figure 23: Cubical building in ABL. Pressure coefficient profiles on the vertical and horizontal sections. RANS and hybrid results on mesh B.
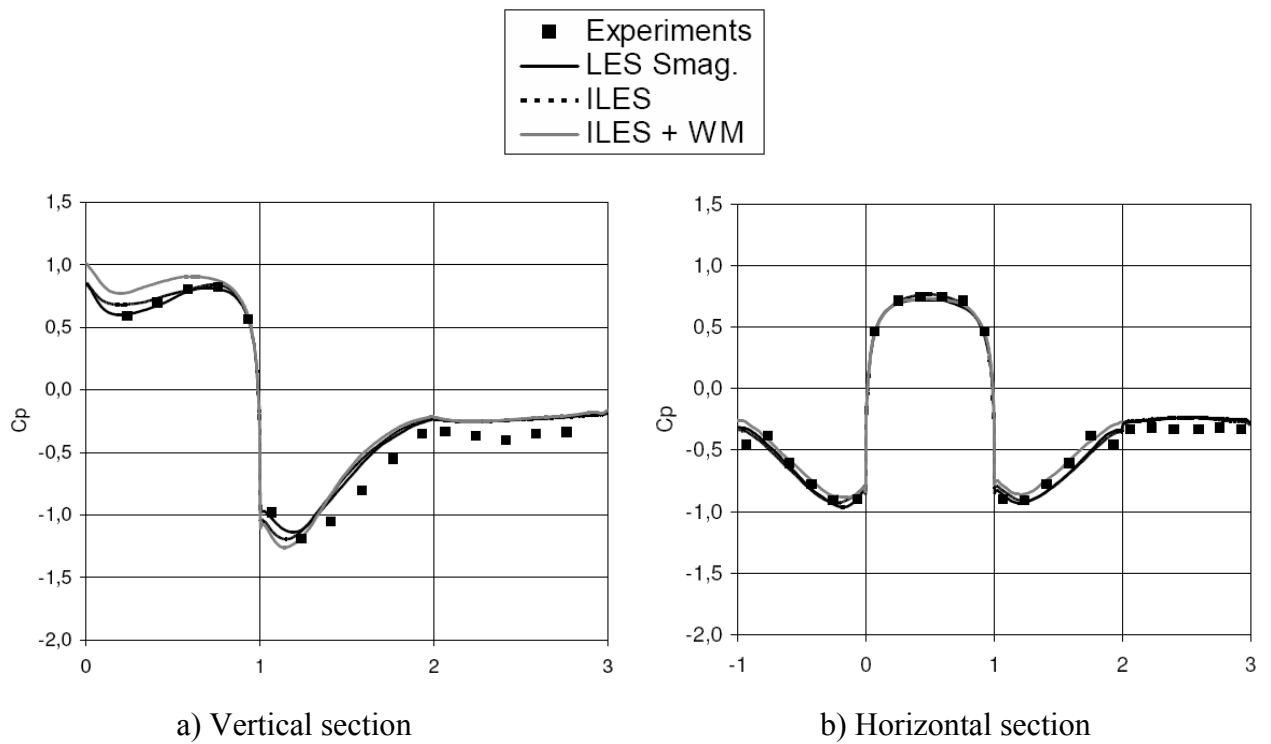

Figure 24: Cubical building in ABL. Pressure coefficient profiles on the vertical and horizontal sections. LES and ILES results on mesh B.

4.7. Sensitivity to blockage and roughness

4.7.1. Sensitivity to domain extension

As already mentioned in section 4.1, we repeated some of the simulations in a domain with bigger dimensions in order to see if significant differences occur. Some RANS and hybrid results on a vertical section on the basic and large domains are shown in figure 25. In the case of RANS, there is almost no difference between the results on both domains. In the hybrid case, some small differences can be observed, in particular at the front of the building (0–1). This is due to the longer upstream length, which causes the oncoming velocity profile to deform somewhat.
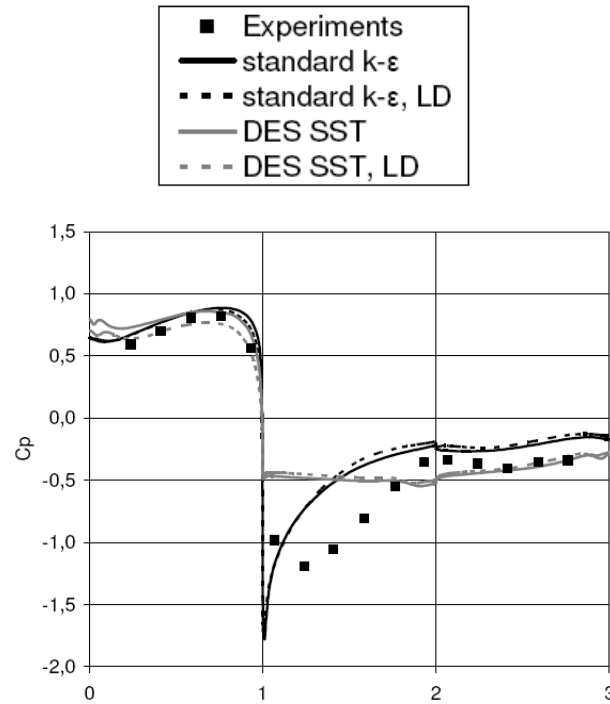

Figure 25: Effect of domain extension on pressure predictions (LD means large domain).

4.7.2. Sensitivity to roughness

Figure 26 shows the effect of roughness applied to the bottom wall of the domain. There is hardly any influence of the roughness on the pressure predictions.
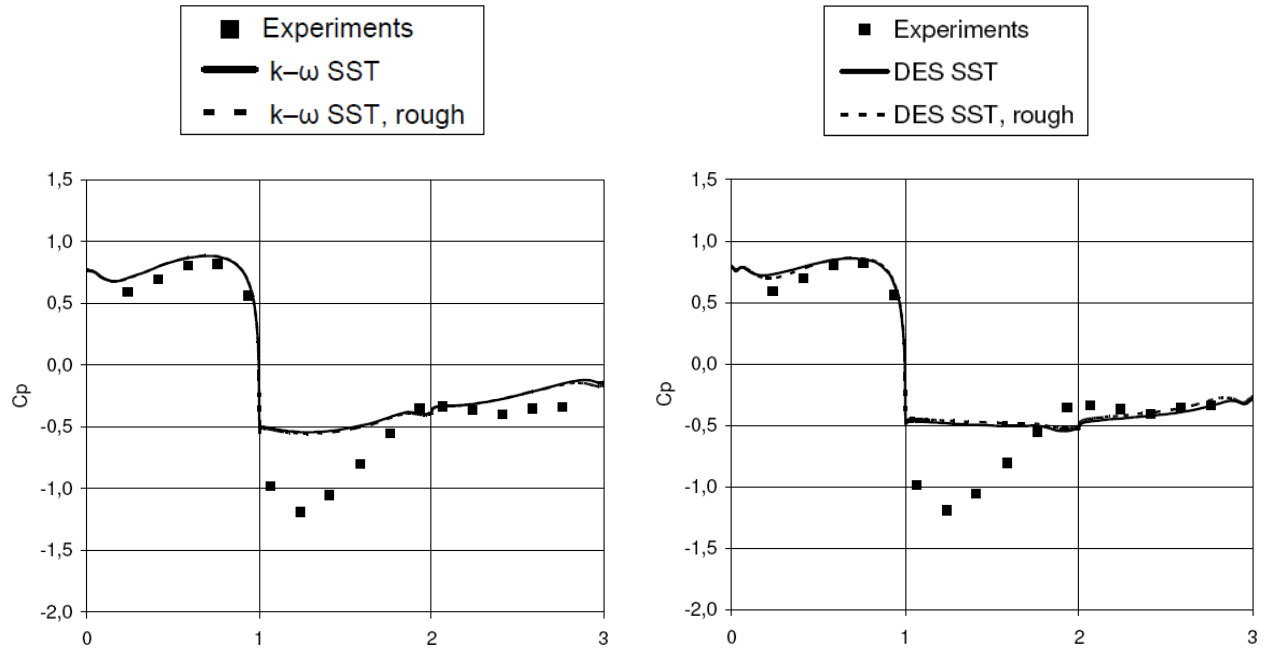
Figure 26: Effect of roughness on Cp predictions.

4.8. Best model for high Reynolds number

The conclusion from the results in figures 17, 18, 22, 23 and 24 clearly is that ILES is the best suited technique for the prediction of the pressure distribution on a building in an atmospheric boundary layer, if a very coarse grid is used.

4.9. Magnitude of the error on the pressure coefficient

Similarly as discussed for velocity profiles in section 3, for the best performing model, which is here the ILES, the general correspondence between the predicted en experimental pressure distributions is visually very good (figure 22 and 24). However, quantitative differences may be quite high. Figure 27 shows the differences between predicted and experimental values of the pressure coefficient for Mesh A. We use the term error to indicate the difference. The maximum difference is in the order of 10% for the vertical section and in the order of 20% for the horizontal section. For mesh B (not shown), the differences are respectively 20% and 10%. The figure also shows the differences for wind tunnel experiments. The wind tunnel data are from Richards et al. (2007) for the vertical section and by Hölscher and Niemann (1998) for the horizontal section. We observe that the maximum difference between field experiments and wind tunnel experiments is of the order of 20% for both the vertical and horizontal sections. This means that the numerical predictions are closer to the field experiments than the wind tunnel predictions. So, in this sense, the numerical predictions can be considered as very successful. The comparison with the wind tunnel data also illustrates that it is very difficult to judge quantitatively on the precision of the numerical simulations. As discussed by Richards et al. (2007), there are big differences in the inflow conditions in the wind tunnel experiments with respect to the field experiments. In the wind tunnel experiments, there is almost no variation in the wind direction, while in the field experiment the variation is very strong. Also, in the wind tunnel experiments, the integral length scale of the incoming turbulence is much smaller than in the field experiment. The same differences occur in the numerical simulations. We conclude from figure 27 that the numerical simulations have the same quality as the wind tunnel experiments. We discuss further the qualities of the numerical predictions in the next section.
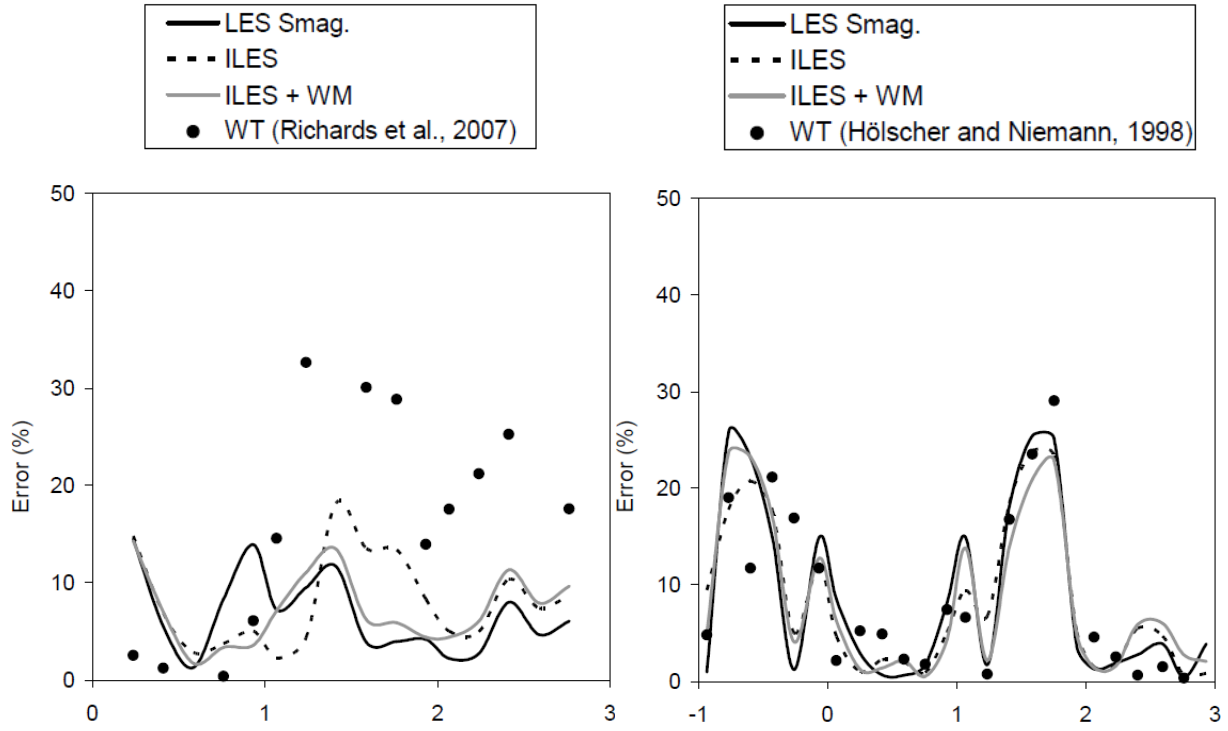
Figure 27: Comparison of errors on mean pressure predictions (left: vertical; right: horizontal section) for Mesh A. Black circles denote wind tunnel data.

5. VARIATION OF C_P WITH WIND DIRECTION ON THE ROOF OF A CUBICAL BUILDING IN AN ATMOSPHERIC BOUNDARY LAYER (ABL)

In one of their experiments, Richards and Hoxey (2008) measured the mean pressure on the roof for various wind directions. Thereto they placed additional pressure taps on one quarter of the roof, as shown in figure 28. For tap 14 and the image tap 41 (black squares in figure 28), they recorded the 12 min mean pressure coefficients for a range of mean wind directions.
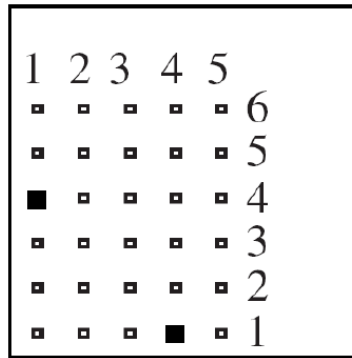

Figure 28: Plan view of the pressure taps on the roof.

We performed simulations for the wind direction 90° and 45°. For the 90° flow, we used mesh A (figure 14). For the 45° flow incidence, a close up of the mesh is drawn in figure 29. The mesh is similar to mesh A, having the same number of cells and maximum expansion ratio.
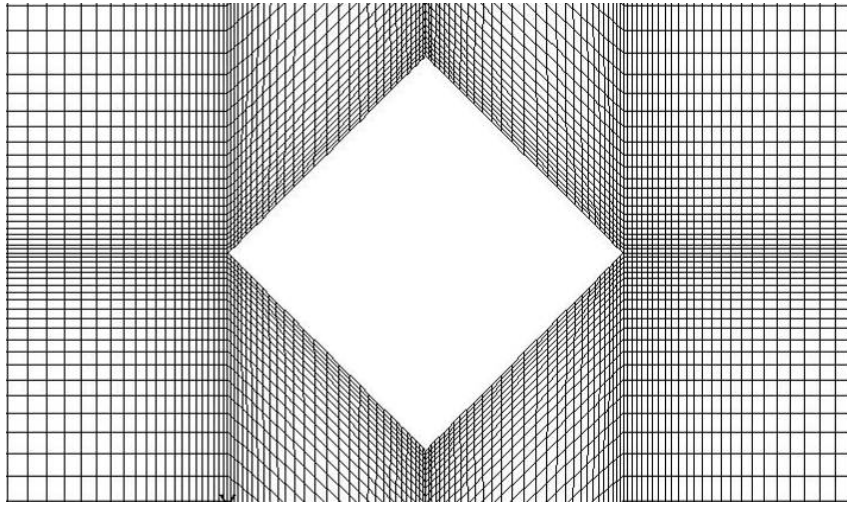
Figure 29: Close up of the grid used for the 45° simulations.

Using these data, and by making use of the planes of symmetry of the cube, the pressure coefficients for tap 14 for wind angles of –45°, 0° and 135° were determined with ILES and with LES with the Smagorinsky–Lilly model (C_S = 0.1). These predicted values are included in figure 30 as black triangles and circles. The hollow squares and diamonds denote the experimental data (digitized from Richards and Hoxey, 2008). It is clear that the predictions are within the scatter of the experimental data points.
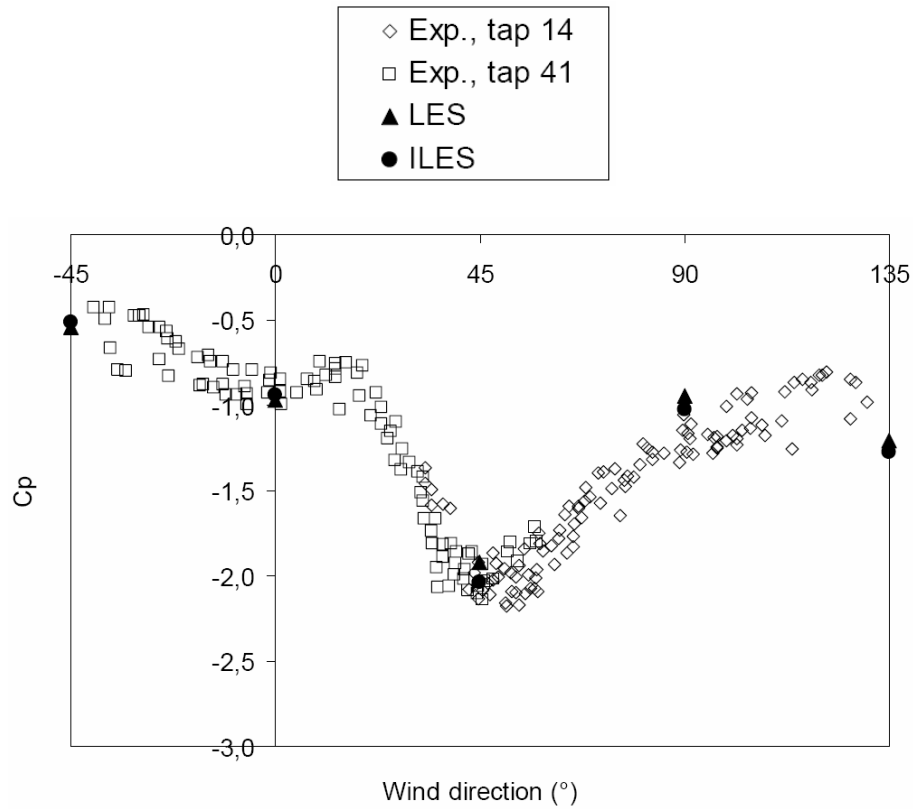
Figure 30: Variation of C_P on the roof for tap 14.

6. CONCLUSIONS

Based on the results of the wind tunnel experiment of Martinuzzi and Tropea, our expectation was that the DES SST model would again perform the best for the cubical building in the atmospheric boundary layer. This is not what we observe. The results of the hybrid RANS/LES simulations are poor and almost equal to the results of the steady state RANS simulations. The main reason for the poor predictions is that the grids which we use are not fine enough for hybrid simulations, so that the modification of the RANS model to serve as a sub–grid model in the LES zone is not fully justifiable. We could make use of much finer grids. This would lead to better predictions but at a large computational cost. This is what we try to avoid here. It is remarkable that we obtain good results on coarse grids with the LES approach. With LES, we also observe only little sensitivity of the quality of the predicted pressure distribution to the grid resolution in wall vicinity and to the wall stress calculation method. Even the sub–grid model has little influence if a TVD scheme is used for discretization of the convective terms in the momentum equations. So, implicit LES functions very well on a very coarse grid. Clearly, for practical prediction of the pressure distribution on real size buildings, implicit LES is recommended.

REFERENCES

Cebeci, T., Bradshaw, P., 1977. Momentum Transfer in Boundary Layers, Hemisphere Publishing Corporation, New York.

Fureby, C., 1999. Large eddy simulation of rearward–facing step flow. AIAA Journal 37(11), 1401–1410.

Fluent 6.3 Documentation, 2006. Fluent Inc., Lebanon, USA.

Germano, M., Piomelli, U., Moin, P., William, H.C., 1991. A dynamic sub–grid scale eddy viscosity model. Physics of Fluids A 3 (7), 1760–1765.

Ghosal, S., Moin, P., 1995. The basic equations for large eddy simulation of turbulent flows in complex geometry, J. Comput. Phys. 118, 24–37

Grinstein, F.F., Drikakis D., 2007. Computing turbulent flow dynamics with implicit large eddy simulation. Journal of Fluids Engineering 129, 1481–1482.

Hanjalic, K., Kenjeres, S., 2008. Some developments in turbulence modelling for wind and environmental engineering. J. Wind Eng. Ind. Aerodyn. 96, 1537–1570.

Hölster, N., Niemann, H.–J., 1998. Towards quality assurance for wind tunnel tests: A comparative testing program of the Windtechnologische Gesellschaft. J. Wind Eng. Ind. Aerodyn. 74–76, 599–608.

Huang, P., Bradshaw, P., Coakley, T., 1993. Skin friction and velocity profile family for compressible turbulent boundary layers. AIAA Journal 31(9), 1600–1604.

Kader, B., 1981. Temperature and concentration profiles in fully turbulent boundary layers. Int. J. Heat Mass Transfer 24 (9), 1541–1544.

Kim, W.–W., Menon, S., 1997. Application of the localized dynamic sub–grid scale model to turbulent wall–bounded flows. Paper AIAA–97–0210, American Institute of Aeronautics and Astronautics, 35th Aerospace Sciences Meeting, Reno, NV.

Leonard, B.P., 1991. The ULTIMATE conservative difference scheme applied to unsteady one–dimensional advection. Comput. Methods Appl. Mech. Engrg. 88, 17–74.

Lilly, D. K., 1992. A proposed modification of the Germano sub–grid scale closure method. Physics of Fluids 4, 633–635.

Lim, H.C., Thomas, T.G., Castro, I.P., 2009. Flow around a cube in a turbulent boundary layer. J. Wind Eng. Ind. Aerodyn. 97, 96–109.

Lun, Y.F., Mochida, A., Yoshino, H., Murakami, S., 2007. Applicability of linear type revised k–ε models to flow over topographic features. J. Wind Eng. Ind. Aerodyn. 95, 371–384.

Martinuzzi, R., Tropea, C., 1993. The Flow around surface–mounted, prismatic obstacles placed in a fully developed channel flow. Journal of Fluids Engineering 115, 85–92.

Mathey, F., Cokljat, D., Bertoglio, J.–P., Sergent, E., 2006. Assessment of the vortex method for large eddy simulation inlet conditions. Progress in Computational Fluid Dynamics 6, 58–67.

Murakami, S., Mochida, A., Kondo, K., Ishida, Y., Tsuchiya, M., 1997. Development of new k–ε model for flow and pressure fields around bluff body. J. Wind Eng. Ind. Aerodyn. 67 & 68, 169–182.

Patnaik, G., Boris, J.P., Young T.R., Grinstein F.F, 2007. Large scale urban contaminant transport simulations with MILES. Journal of Fluids Engineering 129, 1524–1532.

Popovac, M., Hanjalic, K., 2007. Compound wall treatment for RANS computation of complex turbulent flows and heat transfer. Flow, Turbulence and Combustion 78, 177–202.

Richards, P.J., Hoxey, R.P., Short, J.L., 2001. Wind pressures on a 6m cube. J. Wind Eng. Ind. Aerodyn. 89 (14–15), 1553–1564.

Richards, P.J., Hoxey, R.P., 2006. Flow reattachment on the roof of a 6m cube. J. Wind Eng. Ind. Aero. 94, 77–99.

Richards, P.J., Hoxey, R.P., Connel, B.D., Lander, D.P., 2007. Wind–tunnel modelling of the Silsoe cube. J. Wind Eng. Ind. Aerodyn. 95 (9–11), 1384–1399.

Richards, P.J., Hoxey, R.P., 2008. Wind loads on the roof of a 6m cube. J. Wind Eng. Ind. Aero. 96, 984–993.

Rodi, W., 1997, Comparison of LES and RANS calculations of the flow around bluff bodies. J. Wind Eng. Ind. Aerodyn. 69–71, 55–75.

Roy, C. J., DeChant, L. J., Payne, J. L., Blottner, F. G., 2003. Bluff–body flow simulations using hybrid RANS/LES. AIAA Paper 2003–3889.

Sweby, P.K., High resolution schemes using flux limiters for hyperbolic conservation laws, 1984. SIAM J. Numer. Anal. 21, 995–1011.

Tominaga, Y., Mochida, A., Murakami, S., Sawaki, S., 2008. Comparison of various revised k–ε models and LES applied to flow around a high–rise building model with 1:1:2 shape placed within the surface boundary layer. J. Wind Eng. Ind. Aerodyn. 96, 389–411.

White, F., Christoph, G., 1971. A Simple analysis of compressible turbulent skin friction under arbitrary conditions. Technical Report AFFDL–TR–70–133.

Wolfstein, M., 1969. The velocity and temperature distribution in one–dimensional flow with turbulence augmentation and pressure gradient. Int. J. Heat Mass Transfer 12, 301–318.

Yoshizawa, A., 1993. Bridging between eddy–viscosity–type and second–order turbulence models through a two–scale two–scale turbulence theory, Physical Review E 48 (1), 273–281.